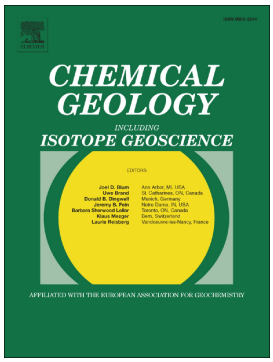

Evolution of chalcophile elements in the magmas of the Bonin Islands

Matthew J. Valetich, John Mavrogenes, Richard Arculus, Susumu Umino

PII: S0009-2541(18)30336-X
DOI: doi:10.1016/j.chemgeo.2018.07.011
Reference: CHEMGE 18839

To appear in: *Chemical Geology*

Received date: 1 December 2017
Revised date: 13 June 2018
Accepted date: 3 July 2018

Please cite this article as: Matthew J. Valetich, John Mavrogenes, Richard Arculus, Susumu Umino , Evolution of chalcophile elements in the magmas of the Bonin Islands. Chemge (2018), doi:10.1016/j.chemgeo.2018.07.011

Title: Evolution of chalcophile elements in the magmas of the Bonin Islands

Author information

Matthew J Valetich. Research School of Earth Sciences, The Australian National University. 142 Mills Rd, Acton ACT 0200. matthew.valetich@anu.edu.au

John Mavrogenes. Research School of Earth Sciences, The Australian National University. 142 Mills Rd, Acton ACT 0200.

Richard Arculus. Research School of Earth Sciences, The Australian National University. 142 Mills Rd, Acton ACT 0200.

Susumu Umino. School of Natural Science, Kanazawa University Kakuma-machi, Kanazawa, Ishikawa 920-1192

Key words: Melt Inclusion; Boninite; Chichijima; Mukojima; Magnetite; Copper; Sulfide Saturation;

Research Highlights

- Chalcophile and trace metal history of boninite series melts tracked in silicate melt inclusions across an extensive compositional range (>18 to <0.5 wt. % MgO)
- Boninite series melts saturate in sulfide despite parental magmas depleted in S
- Direct evidence of co-precipitation of magnetite and sulfide linked to changes in V and Cu previously inferred as sulfide/magnetite saturation

Abstract

Melt inclusions and submarine volcanic glasses and of Boninitic composition are well preserved in beach sands from the islands of Chichijima and Mukojima along the Bonin Ridge. Volcanic glass as well as orthopyroxene and spinel hosted melt inclusions in these sands span almost the entirety of

boninite series melt compositions ranging from >18 wt. % to <0.5 wt. % MgO. Copper, V and other trace metals were tracked over the entirety of the boninite range and when compared to other suprasubduction melts from the Manus and Lau basins, highlight the variability of these elements across different arc magmas. Boninite series melts show similar behaviour of Cu and V to melts from the Manus and Lau basins, suggestive of magnetite (saturation)-triggered sulfide saturation (a 'magnetite crisis'). Furthermore, a direct link of these geochemical trends to physical sulfides and magnetite in sample material has been established for the first time. Comparisons of incompatible trace elements suggests that sulfide saturation in the boninite series melts occurred after less fractionation (earlier) than either the Manus or Lau basin melts. This is surprising, given secondary melts such as boninites are generated from melt-depleted mantle sources and are thought to contain very little S. Indeed S contents of melt inclusions of primitive boninitic composition are less than half that of the primitive Manus basin melts. While the mechanism of sulfur enrichment in the boninite series melts remains a mystery, the oxidised nature of the Bonin ridge boninites suggests that magnetite-triggered melt reduction is necessary to stabilise sulfide. Finally the timing magnetite crises generally may be mostly controlled by magmatic oxidation state and total iron contents.

1. Introduction

In the last 30 years, in situ microanalytical techniques have allowed advances in our understanding of magmatic systems, with the majority of elements now measurable at parts per million to parts per billion levels. Nevertheless, many magmatic systems have not been analysed for chalcophile elements. Our understanding of these elements is limited to detailed studies of a handful of arc magmas [e.g., Jenner et al., 2010;2012;2015; Park et al., 2015], spanning a limited compositional range of these melt types [Schmidt and Jagoutz, 2017]. Nevertheless, the behaviour of these elements during magmatic differentiation is important to our understanding of ore-forming processes, particularly in convergent margin magmas. The most topical and significant of these deposit types, the porphyry-epithermal Cu-Au-Ag-Mo systems (referred to here as porphyry deposits), currently supply the vast majority of the world's Cu as well as Mo, Au, Ag, and base metals

(Sillitoe, R., 2010). The link between subduction-related magmatism and porphyry deposit formation is undoubted, however the vast majority of subduction-related magmas do not form porphyry deposits and the factors controlling the fertility of individual arc systems are unclear. It is well established that arc melts stand unique from those formed in other settings due primarily to the contribution of volatiles from the subducting oceanic lithosphere (e.g., Arculus 2004). However, the nature of the contribution from the subducting slab varies and a range of chemically unique melts are produced in convergent margin settings (Arculus & Powell, 1986). These differences have led some to conclude that starting melt compositions ultimately dictate whether or not a porphyry deposit forms (Mungall, 2002; Sun, et al., 2011). Conversely, the complicated and varied evolutionary paths that arc melts follow suggests that fractionation plays a significant role in determining if a magma will produce an ore deposit or not (Richards, 2003; Jenner et al., 2010, 2015; Park et al., 2015).

Conventional models of porphyry deposit formation suggest that magmas, ranging from basalt to dacite, transport the necessary components required to form a porphyry deposit (Lowell and Guilbert, 1970; Burnham, CW., 1994; Hedenquist and Lowenstern 1994). Exsolution of volatiles and metals occurs due to depressurisation and eventual mixing with groundwater in the shallow crust leads to the formation of a porphyry deposit. However, it is unlikely that only a single magma is involved. Famously, porphyry deposits have been referred to as sulfur anomalies (Hunt, 1977) or sulfur deposits with associated metals (Blundy et al., 2015), yet pre-eruptive sulfur concentrations in many dacitic-rhyolitic arc melts record low sulfur (<200ppm) (Hattori and Keith, 2001; Blundy et al., 2015 and references therein). There is also a well-established decoupling of S and Cl over a range of P-T- fO_2 conditions reported in both natural and experimental studies (Lesne, et al., 2011; Wallace, P., 2005). Furthermore, the typically oxidised nature of arc magmas, used to explain the retention of metals from deep to shallow crust is contrasted with the reduced metal-sulfides that typify porphyry deposits (Blundy et al., 2015). One possible mechanism that accounts for these collective observations is initiated by the early release of sulfur from mafic arc melts (Wilkinson, 2013). This

would inhibit sulfide saturation and maintain the incompatible behaviour of metals as melts ascend through the crust and fractionate towards andesitic and more evolved (higher-SiO_2) compositions. Multiple generations of mafic melt might then provide a long-term source of sulfur for an overlying porphyry deposit via a range of possible mechanisms (Henley et al., 2015; Blundy et al., 2015; Mavrogenes and Blundy, 2017). There are tens of kilometres of separation between the initial depth of arc magma generation (Schmidt & Jagoutz, 2017) and the depth of emplacement of porphyry deposits. Therefore, constraining what occurs at depth is vital if we are to identify processes that occur in the shallow crust where porphyry deposits form.

Studies of the arc-proximal Eastern Manus Backarc Basin (EMBB; Papua New Guinea) and southern Valu Fa Ridge in the Lau Basin, Tonga (SVFR), suggest that under-saturation of sulfur in primitive arc magma combined with the relatively high oxidation state of evolved arc magmas (0-2log units above the fayalite-quartz-magnetite (FMQ) buffer) delays sulfide saturation (Jenner et al., 2010;2015). Oxidised sulfur species do not form compounds that sequester chalcophile elements, such as Cu, Ag, Au and Se, such that these elements are retained in oxidised silicate melts. In more reduced melts where sulfide is stable, chalcophile elements by definition are captured by sulfide melts/minerals. The EMBB and SVFR magmas show a significant build-up of chalcophiles before a marked decline in abundance at 3-4 wt. % MgO (60 wt. % SiO_2). This decline is concurrent with a similarly drastic change in V/Sc, attributed to saturation in magnetite (Sun et al., 2003; 2004). Jenner et al (2010) conclude that the change in $Fe^{3+}/\sum Fe$ caused by magnetite saturation drops fO_2 sufficiently to stabilise sulfide, a process they termed the “magnetite crisis”. The behaviour of chalcophile elements in the EMBB suite contrasts markedly with their behaviour in mid ocean ridge basalts (MORB) (Jenner and O’Neill, 2012). High sulfur and relatively low fO_2 (FMQ or below) results in early and persistent sulfide saturation in combination with high Fe contents that limits the variability of chalcophile concentrations in MORB. Park et al. (2015) interpret the behaviour of platinum group elements in Tonga rear arc magmas as the results of favourable timing of volatile exsolution relative to magnetite-triggered sulfide saturation. A redox-controlled delay in sulfide saturation enables

metals to partition into and become mobilised in the volatile phase before it is lost to the sulfide. What remains unknown is if the magnetite crisis is a feature common to supra-subduction melts, and furthermore, if the presence or absence of this "crisis" controls magma fertility for forming ore deposits.

In this paper, we show that Cu concentrations determined for a broad compositional range of boninite series glasses and glassy melt inclusions (MINCs) from Mukojima and Chichijima on the Bonin Ridge of the Izu-Bonin arc track chalcophile enrichments and sulfide saturation in the suite. The chalcophile element abundance patterns are broadly similar to those of the EMMB and SVFR. For example, boninite MINCs and glasses show an approximately two-fold increase in Cu concentration before a sudden drop. Vanadium decreases in abundance at slightly higher Mg numbers/lower SiO_2 than Cu. However, these sudden changes in concentration occur at lower Mg and higher Si content than either the EMMB or SVFR melts, and Cu concentrations immediately prior to sulfide saturation are lower. The key differences here lie in the initial composition of the melt and subsequent evolution due to fractional crystallisation, magma mixing or contribution of volatiles from underlying magmas. Melt inclusions provide the only samples of primitive boninite melts on the Bonin Ridge and therefore direct measurements can clarify differences between this melt type and more abundant arc magmas. Key questions addressed here are the relative importance of starting composition versus fractionation in controlling sulfide saturation in suprasubduction zone magmas.

1.2 Geological Background

Boninites are andesitic rocks (53-65 wt.% SiO_2) characterised by >8% MgO and <0.5 wt.% TiO_2 (Le Bas, 2000) sourced from mantle depleted by prior melt extractions on the order of 10-30% (Crawford et al., 1989; Parkinson & Pearce, 1998; Dobson, et al., 2006; Umino et al., 2018). Melting of such refractory mantle should generate melts lower in incompatible elements than MORB. However, enrichments in LREE, Zr, Sr (but not Nb and Ta) and radiogenic Pb compared with MORB is

consistent with superimposed enrichments via fluids from an associated subducted slab (Umino et al 2015; Falloon and Danyushevsky, 2000; Konig et al., 2010; Cameron, 1983; Stern et al., 1991; Bryant et al., 2003).

The multi-component sources of primitive boninites provides an opportunity to explore the behaviour of trace elements derived from both mantle and slab. For example, HFSE and LILE ratios such as Ba/Th, Nb/La and Sb/Ce have been used to discriminate fluid and melt components of boninite lavas from PNG and Cyprus (Konig et al 2010). Given the incompatible behaviour of chalcophile elements such as Cu, Ag, Se and S during partial melting of the mantle (Fellows & Canil, 2012; Wang & Becker, 2015) it is likely that primitive boninites are depleted in chalcophile elements. Any enrichments could then be attributed to slab-derived melt inputs (Mungall, et al, 2002; Li et al., 2011). Comparisons between the most magnesian basalts from the Manus and Lau Basins and MORB, however, show Cu concentrations are similar, leading to the conclusion that slab contributions of chalcophile elements in the former are negligible (Jenner et al., 2015).

1.2 Geological Background

The Izu-Bonin Mariana (IBM) intra-oceanic arc extends for ~2500km southward from Japan, comprising the Izu-Bonin arc in the north and Mariana arc to the south, terminating just south of Guam (Ishizuka et al., 2006). Location maps for Mukojima and Chichijima are presented in Kanayama et al. (2012) and Umino, (1986) respectively. A brief history of the arc is outlined in Arculus et al. (2015). Subduction of the Pacific plate beneath the Philippine Sea plate initiated at 52Ma, accompanied by generation of low-Ti tholeiitic basalts (so-called fore-arc basalt of Reagan et al., 2010); the first boninite melts were erupted at about 48Ma (Ishizuka et al 2011). East of the current volcanic front in the Izu-Bonin arc is the Bonin Ridge, which extends for about 400km, striking north-south with a maximum width of just over 100km (Ishizuka et al., 2006). Subaerial exposures along the Bonin Ridge are the type localities for boninite rocks with the Mukojima (“bridegroom”) group in the northern part of the ridge, the Chichijima (“father island”) group in the centre, and the Hahajima

("mother island") group to the south (Kanayama et al 2012). The western margin of the Bonin Ridge is the steep Bonin escarpment with more than 3 km of relief, likely formed during Oligocene rifting that formed the immediately proximal Ogasawara Trough (Ishizuka et al., 2006 and references therein). The Bonin Ridge and escarpment exposes early subduction stratigraphy for the region and has been characterised in detail (e.g. Ishizuka et al., 2006, 2011. Reagan et al., 2010; Reagan et al., 2017) and may be summarized from bottom to top as; 1) mantle peridotite, 2) gabbro, 3) sheeted dykes, 4) basaltic pillow lavas (forearc basalt), 5) boninite series rocks 6) tholeiites and calcalkaline lavas. $^{40}Ar/^{39}Ar$ ages indicate the bulk of boninite formed between 48 and 46Ma (Ishizuka et al., 2006) and are present on both Chichijima and Mukojima island groups. Later (~45Ma), high magnesian andesites outcrop on the northern parts of Chichijima and in the Hahajima Island group in the Mikazukiyama Formation (Kanayama et al., 2012). Boninite series rocks include both primitive boninites as well as evolved, high-Mg dacitic and rhyolitic rocks of boninitic affinity. Melting of increasingly melt-depleted (increasingly lower modal clinopyroxene) but slab-enriched mantle results in a range of major element compositions which have been classified into four groups; high-Ca boninites and types 1-3 of low-Ca boninites, as detailed by Crawford et al., (1989). Boninites from the IBM arc are dominantly low-Ca boninites (typically types 1 and 3) but can have CaO/Al_2O_3 ratios more akin to high-Ca boninites, albeit with much lower total CaO than those of the Troodos boninites (e.g. Cameron, 1985) on which the high-Ca classification was originally based (Crawford, 1989).

Boninites from the Bonin archipelago are divided into high-Si and low-Si types (Umino et al., 2015 and references therein). The majority of 46-48 Ma boninites are high-Si, typically with low CaO, high Zr/Ti, and severely depleted but concave-up, chondrite-normalised rare earth element (REE) abundance patterns. These characteristics are attributed to high temperature (>1400^{o}C) melting of refractory (≤30% prior melt extraction), harzburgitic mantle fluxed by slab-derived fluids and melts (Umino et al., 2015; 2018). Low-Si boninites are of two types, one of which coexists with the 46-48 Ma high-Si boninites and another found in the 45 Ma Mikazukiyama formation. The latter are high-

Ca boninites (Umino et al., 2015) and not discussed further in this contribution. Low-Si boninites are characterised by variable composition; 6-11% CaO, CaO/Al_2O_3 0.5-1 and Zr/Ti 0.01-0.03 (Umino et al., 2015) and REE abundances consistent with derivation from a depleted lherzolite mantle source (11-20% prior melting) as well as a significant slab-fluid contribution (Umino et al., 2015; 2018). Much of the pre-boninite magmatism along the Bonin Ridge is the MORB-like forearc basalt (FAB), generated during the earliest stage of IBM subduction inception (Reagan et al 2010). Hydrous melting of the FAB residue is proposed as the source of 46-48 Ma low-Si boninite magmatism (Umino et al., 2018).

Petrographic observations show that spinel and olivine are the first crystallising phases, followed by, orthopyroxene, clinopyroxene, magnetite and plagioclase. Bulk compositions of the 48-46 Ma boninite series rocks from Mukojima and Chichijima are published in Umino (1986) and Kanayama et al. (2012). Models of fractional crystallisation of high- and low-Si boninites show that olivine followed by orthopyroxene and finally clinopyroxene dominate compositional evolution. Spinel is typically Cr-rich with Cr# (Cr/Cr+Al) >0.89 and >0.85 for high and low-Si boninites respectively (Umino et al., 2015) while olivine and orthopyroxene mostly have Mg# ($100*Mg/Mg+Fe^{2+}$) >85 (Umino, 1986; Kanayama et al., 2012). Clinopyroxene, magnetite and plagioclase all saturate relatively late in the crystallisation sequence, and in some cases plagioclase is only present as microcrysts in groundmass glasses (Dobson et al., 2006).

2. Samples and analysis

2.1 Samples

Mukojima, ~70 km NNW of Chichijima, is dominated by bedded tuff breccia and pillow lavas of boninite composition (Kanayama et al., 2012). Natural mineral concentrates from beach sands are the primary samples analysed (Umino et al., 2015). Those from Minamihama, on the western side of Mukojima (Location M1-03 in Figure 6 (Kanayama et al., 2012)) are composed of orthopyroxene crystals with lesser proportions of Cr-spinel, magnetite, clinopyroxene, olivine, plagioclase, and

fragments of glass. Concentrates from both the 48-46 Ma high- and low-Si boninites in the Maruberiwan formation of Chichijima were also sampled (Umino, 1986). Mineralogies are similar to those from Mukojima, dominated by orthopyroxene, with lesser Cr-spinel and magnetite and rare clinopyroxene, plagioclase, and fragments of erupted glass. All mineral phases present in the sands of both Chichijima and Mukojima contain rare to abundant MINCs which range in size from <10µm to >100µm across. Olivine typically contains smaller MINCs (<10µm) while orthopyroxene, clinopyroxene, Cr-spinel, magnetite, and plagioclase contain larger MINCs. The MINCs have a wide range of assemblages, from glass-only through glass plus gas bubbles, to glass with varying proportions of heterogeneously trapped (stable), daughter (formed post entrapment (meta-stable)) and quench (unstable) crystallites. Orthopyroxene fractionation persists across a broader range of melt compositions than any other phase and not surprisingly, is also the most abundant phase in the mineral sands. Clinopyroxene is rare, while olivine and plagioclase are markedly sparse. Spinel (both Cr and Fe rich) is concentrated in the sands compared to the volumetrically minor phase it would have represented in the melt, likely due to natural reworking, sorting and concentration processes. Orthopyroxene- and spinel- (Cr-spinel and magnetite) hosted MINCs were targeted for this study as together they cover the entire boninite compositional series and provide abundant sample volumes for generation of a statistically-meaningful dataset. The MINCs in Cr-spinel are predominantly spherical, elliptical and tetragonal (negative crystal)-shaped inclusions, trapped along growth zones reflecting a primary origin. Post-entrapment crystallisation (PEC) of olivine and pyroxene in Cr-spinel-hosted inclusions is most common as radiating and interlocked quench crystals, sometimes interspersed with bubbles and only interstitial glass remaining (Figure 1). Less common are glass-dominated inclusions with rims of skeletal pyroxene. Some Cr-spinel-hosted inclusions are entirely glass with one shrinkage bubble. Orthopyroxene hosts primary and secondary or pseudo-secondary melt inclusions. Primary melt inclusions appear as spherical or elliptical inclusions, mostly along growth zones. Secondary or pseudo-secondary inclusions are small and abundant along fractures. Clinopyroxene crystals are common within orthopyroxene-hosted MINCs, and rarer magnetite and

plagioclase crystals along with sulfides are limited to evolved, Fe-rich orthopyroxene hosts. Clinopyroxene is present as either euhedral micro-crystals or as feathery crystals along inclusion rims. Large euhedral pyroxene and plagioclase crystals are considered to be trapped crystals. A single shrinkage bubble is typical of orthopyroxene-hosted MINCs, with few exceptions. A small proportion of orthopyroxene-hosted MINCs contain sulfide and carbonate crystals on the walls of the shrinkage bubble, however Raman spectroscopy shows the vast majority of shrinkage bubbles are likely to be empty. Inconsistent proportions of glass and magnetite/plagioclase/sulfide suggest that both heterogeneous inclusion/entrapment of crystals as well as post-entrapment crystallisation (forming daughter crystals) are occurring (Figure 2). Magnetite-hosted melt inclusions often contain trapped microcrystalline apatite, clinopyroxene, and plagioclase with lesser sulfide. Daughter crystals are dominantly plagioclase and apatite with rare sulfide. Shards of erupted glass (common in sands from Mukojima and less so from Chichijima) of high-Mg andesitic to dacitic composition contain phenocrysts of Fe-rich orthopyroxene, clinopyroxene, and magnetite. Rare phenocrystic plagioclase is also present, but plagioclase is most common as microcrystals. Microcrystals dominated by plagioclase, pyroxene, and lesser magnetite vary from less than 5% to over 50% of the groundmass and can include skeletal pyroxenes and magnetite formed during quenching.

There is clear evidence for both trapping of sulfides and post-entrapment sulfide saturation in MINCs. Post-entrapment sulfide saturation in silicate melt inclusions is invariably preceded by crystallisation of silicate and oxide phases and multiple inclusions in the same host display similar proportions of daughter phases. Perfectly spherical sulfides suspended in glass or included in other daughter phases demonstrates sulfide immiscibility in the silicate melt as it quenched. In addition, other sulfides with a crystalline appearance occur on the surfaces of magnetite crystals (figure 3) and both modes of sulfide morphology can be found in the same MINC. The latter morphologies likely result through localised melt reduction immediately adjacent to growing magnetite crystals resulting in localised sulfide saturation (Anenburg and Mavrogenes, 2016) while the immiscible sulfide droplets are the result of sulfide saturation of the entire inclusion. Both modes of sulfide morphology are also trapped

without silicate melt, demonstrating that post entrapment processes are likely reflective of large scale magmatic processes. Crystalline sulfides are found as inclusions in magnetite phenocrysts or in plagioclase and pyroxene phenocrysts in contact with magnetite. Spherical or elliptical sulfide melt inclusions are found in magnetite, plagioclase and pyroxene phenocrysts usually with no other phases, or sometimes variably trapped with minor portions silicate melt and silicate minerals demonstrating that the sulfide did not form after entrapment.

2.2 Homogenisation Experiments

Homogenisation experiments were conducted on MINCs from Mukojima and Chichijima to better understand and reverse effects of PEC. Heating of orthopyroxene-hosted melt inclusions was done on a Linkam TS1400XY heating stage under either atmospheric conditions or in a nitrogen atmosphere. Heating rates were tested from 50°C/minute down to 1°C/minute to ensure there was no overheating from kinetic lag (Danyushevsky et al., 2002). The MINCs were heated until bubble disappearance which was recorded as the temperature of homogenisation (T_h), before rapid cooling. Above 1160°C, the host crystals began to glow and in some instances MINC visibility was completely lost by 1190°C. If homogenisation had not occurred by the time visibility was lost, heating continued, before the sample was cooled and checked for homogenisation. Each successive sample was heated 20°C higher than the previous sample if it had not homogenised. Samples were heated up to 1400°C. Inclusions were heated only once to avoid H-loss from repeated heating, which increases T_h (Massare et al., 2002). The use of the Linkam heating stage was simply to establish T_h. Samples used for heating stage experiments were not in an fO_2-controlled atmosphere, nor were they quenched in water but removed from the heating stage and cooled quickly. The opaque nature of Cr-spinel inclusions precludes their use with this technique.

Batch heating of mineral separates was done in a 1 atmosphere pressure furnace buffered with a CO_2-CO mix equal to 0.5 log units below FMQ at maximum temperature. Orthopyroxene separates were heated at 1200, 1250, and 1300°C corresponding to the range of homogenisation

temperatures recorded on the Linkam heating stage as well as previously reported T_h for orthopyroxene-hosted, boninitic melt inclusions (Danyushevsky et al., 2002). Cr-Spinel separates were heated to 1300, 1350, 1400 and 1450°C. Two heating techniques were used. Firstly a uniform 6°C/min heating rate was used and inclusions were kept at temperature for 1hr before quenching in water. Secondly, heating at 6°C/min until approximately 1100°C, before rapid heating at 120°C/min until T_{max}. Samples were held at T_{max} for 5 minutes before rapid quenching into water. Rapid heating above 1100°C and short dwell time is aimed at reducing the time at which the samples are at high temperatures to minimise diffusive re-equilibration and H-loss (Danyushevsky et al., 2002; Massare et al., 2002).

2.3 Analysis

Single grains of Cr-spinel, pyroxene and magnetite were mounted in 2.5 cm-wide epoxy disks and singly polished to a grit size of 0.25 µm to expose MINCs. Observation of samples under reflected and transmitted light enabled selection of inclusions with minimal daughter crystals and no visible leaks, alteration, or decrepitation. Those MINCs containing shrinkage bubbles with crystallised rims were also discarded on the assumption that degassing into the shrinkage bubble had occurred (Kamenetsky & Kamenetsky 2010). Glass shards were set in 2.5 cm epoxy mounts and singly polished to 0.25 µm before selection of the most microcryst-free shards.

Quantitative energy dispersive spectroscopic (EDS) analyses were carried out on the Hitachi 4300 SE field emission scanning electron microscope (FE-SEM) at the Centre of Advanced Microscopy, Australian National University (ANU). The FE-SEM was equipped with an integrated Oxford X-max element detector operated at 15 kv, 25 mm working distance with a 0.6 ampere current. Well characterised mineral standards were used for calibration. EDS analyses were used to quantify homogenised melt inclusion composition, as well as to identify zoning in host crystals proximal to melt inclusions and characterise daughter phases in melt inclusions. Electron microprobe wavelength dispersive spectroscopic (WDS) analyses of glasses as well as Cr-spinel pyroxene- and

magnetite hosted MINCs were undertaken on the JEOL JXA8200 and JEOL JXA-8530F Plus electron probe micro-analysers (EPMAs) for major and some minor elements at the Advanced Analytical Centre at the James Cook University, Queensland and Centre of Advanced Microscopy at the Australian Nation University, the Australian Capital Territory respectively. The EPMAs were operated at 15 kV and a 20 nA beam current, with a defocussed beam of 5 and 10 µm. Melt Inclusions hosted in orthopyroxene and Cr-spinel with shrinkage bubbles preserved sub-surface were analysed using Raman micro-spectroscopy at the Research School of Physics and Engineering (ANU) for vapour phases in the shrinkage bubble. A Renishaw inVia Reflect Spectrometer System equipped with a standard confocal microscope was used for Raman spectral analysis. A Renishaw diode-pumped solid state laser provided 532 nm laser excitation with 5 mW power at the sample. A 2400 grooves/mm grating was used giving a spectral resolution of 0.5 cm^{-1}. Single Raman spectra were obtained using a 1 second integration time and 10 to 30 accumulations using a 100x Leica microscope objective. All analyses were performed as an automated procedure using the Wire version 4.2 software. Glasses and MINCs hosted in Cr-spinel, pyroxene and magnetite were analysed for trace elements by laser ablation inductively coupled plasma mass spectrometry (LA-ICP-MS) at the Research School of Earth Sciences (ANU). The system comprises a Lambda Physik COMPex 110 excimer laser (λ = 193 nm), HelEX ablation cell and an Agilent 7700 ICP-MS spectrometer. The analyses were completed using varied spot sizes from 22-105 µm and a laser pulse rate of 5 Hz. Each analysis included 20 seconds of background and 40 seconds of ablation time. Traverses across exposed melt inclusions at 0.5 µm and 1 µm/sec were also made using a 50 µm x 6 µm slit and a laser pulse rate of 5 Hz. Each traverse included 20 seconds background. NIST 610 glass (Jochum et al., 2011) was used as the primary standard and NIST 612 glass was the secondary standard for all elements with ^{29}Si as the internal standard.

2.4 Rhyolite-MELTS modelling of boninites

The evolution of boninite series melts were simulated using the modelling software Rhyolite-Melts, which is suitable for silicate-rich, fluid bearing magmatic systems (Gualda et al., 2012). The starting composition was approximated from primitive boninite melt inclusions and adjusted to a liquidus composition calculated within the software using published values for fO_2, P, T and H_2O content (Umino et al., 2015). Starting water contents were 2-5 wt % and fO_2 was initially set to FMQ - FMQ+2, but not constrained during fractional crystallisation simulations. Initial temperature was calculated using the software and varied from 1434 to 1424.3 C with H_2O content. Initial pressure was set to 5600 bar and temperature was allowed to decrease in 2°C increments to 800°C with pressure changes of 0-10 bar per degree C. The starting composition and conditions of the simulation that produced trends that best fit the geochemical data and petrological observations are summarised table 2.

3.1 Homogenisation Experiments

Orthopyroxene-hosted MINCs heated to 1200°C mostly failed to homogenise with daughter phases remaining in >50% of heated inclusions. Similarly, Cr-spinel-hosted MINCs heated to only 1300°C failed to homogenise. Orthopyroxene-hosted MINCs were largely decrepitated by 1400°C, while heating to 1300-1400°C often resulted in over-dissolution of the host and development of serrated edges at inclusion rims. Similarly, Cr-spinel-hosted MINCs heated to 1450°C displayed evidence of over-dissolution. Orthopyroxene-hosted MINCs heated to 1250-1300°C and Cr-spinel-hosted MINCs heated to 1350°C provided the greatest success. Success of homogenisation was assessed as the lowest temperature of heating that yielded MINCs with no daughter phases and no evidence of over-dissolution. Furthermore, MINCs deemed to be successfully homogenised have major element compositions that match trends defined by analyses of bulk rock samples (Kanayama et al., 2012), glass samples, and unheated, glassy, Cr-spinel-hosted MINCs. In the vast majority of cases, the shrinkage bubble reappeared after cooling and there was no apparent correlation between the

different cooling rates or the maximum temperature of heating (T_{max}) and whether or not the bubble was preserved. This is indicative of plastic deformation of the host crystals (Schiavi et al., 2016).

3.2 Major Elements

Silicate MINCs, glasses and mineral compositions are shown in Figure 4 and representative analyses are shown in table 1.The most magnesian compositions were obtained from Cr-spinel-hosted MINCs which contain ~54-58 wt.% SiO_2, 19 – 12 wt.% MgO, 4.6-6.7 wt.% CaO, 6.3-8.3 wt.% Al_2O_3, and 7.7-10.1 wt.% FeO_T (Total Fe displayed as FeO). Orthopyroxene-hosted MINCs have more evolved compositions, containing ~56-70 wt. % SiO_2, 14-0.3 wt. % MgO, 2-9 wt. % CaO and 7 -12.5 wt. % Al_2O_3. The range of compositions of orthopyroxene-hosted MINCs overlaps well with the glasses, serving as an excellent basis for comparison. Glasses contain ~56-67 wt. % SiO_2, 0.3-8.9 wt. % MgO, 4.9-10.4 wt. % CaO and 10-16.5 wt. % Al_2O_3. CaO/Al_2O_3 is between 0.65-1 for all MINC and glass analysed except for the evolved glass samples (<5wt. % MgO). The excursion to lower CaO/Al_2O_3 in evolved glasses is likely due to fractional crystallisation of clinopyroxene. There is generally a change in major element behaviour between 5-6 wt. % MgO and 58-60 wt. % SiO_2. FeO and CaO increases with decreasing MgO until 5-6 wt. % MgO after which CaO and FeO decrease with decreasing MgO. At the same point, CaO/Al_2O_3 decreases and FeO/MgO increases sharply with decreasing MgO. Al_2O_3 consistently increases with decreasing MgO between 18.9 and approximately 0.5 wt. % MgO before beginning to decrease.

Rhyolite-MELTS simulations of fractional crystallisation agree well with the major element geochemical data (figure 4) as well as the petrological observations of Bonin Ridge boninites (e.g., Dobson et al., 2006; Kanayama et al., 2012). The initial fractionating phase is olivine, followed by spinel (Figure 5). Orthopyroxene becomes the dominant fractionating phase at approximately 13-14 wt. % MgO. Clinopyroxene emerges as the dominant fractionating phase at approximately 4-5 wt. % MgO heralding a drop in CaO. The initial spinel phase is Cr-rich, but changes with increasing fractionation towards a magnetite rich end- member. A sharp drop in FeO_T at 1-2 wt. % MgO

coincides with the dominance of the magnetite end-member in the fractionating spinel phase. Oxygen fugacity decreases at a faster rate as the fractionating spinel composition becomes more magnetite-rich. Plagioclase is the last fractionating phase to appear on the solidus at approximately 1 wt. % MgO, reflected by a drop in Al_2O_3.

3.3 Trace Elements

All glass analyses have concave-upward, 'dish'-shaped, chondrite-normalised REE patterns with heavy REE (e.g. Yb) at very low concentrations (Figure 6). Typically, Zr/Ti is between 0.022 and 0.03 with only the most evolved glasses having Zr/Ti up to 0.035. Ba/Th is between 283 and 389 while Th abundances are 0.11-0.18 ppm. The majority of glass analyses have trace element compositions consistent with the 46-48 Ma low-Si boninites, with few analyses falling into the high-Si group (Umino et al., 2015). Limited REE analyses of Cr-spinel- and orthopyroxene-hosted MINCs have Zr/Ti of 0.022-0.029 and similar chondrite-normalised and MORB-normalised REE patterns as the glasses, consistent with their belonging to the same magmatic system. Currently there are no REE data for magnetite-hosted MINCs, however, given the agreement seen among major and trace element analyses, it is likely the magnetite hosted inclusions are of the same system.

The most primitive boninite compositions contain <50 ppm Cu, 65-75 ppm Zn, 136-229 ppm V, 29-41 ppm Sc and 48-300 ppm Ni (Figure 7). Ni is variable and decreases rapidly with decreasing MgO. Zinc and Sc increase with decreasing MgO until approximately 8 wt. % MgO, after which Sc decreases with MgO, while Zn remains relatively constant. V increases in concentration between 15 wt. % MgO and 3-5wt. % MgO before dropping. Cu increases by approximately 10 ppm between 18.5 and 11.5 wt. % MgO, but between 11.5 wt. % and 1-2 wt. % MgO, Cu approximately doubles in concentration to ~120 ppm, before declining rapidly in abundance.

4. Discussion and Conclusion

4.1 Homogenisation Experiments and PEC

Estimated homogenisation temperatures for orthopyroxene (1250-1300°C)- and spinel (~1350°C)-hosted MINCs agree with homogenisation temperatures previously published for boninite MINCs (Danyushevsky et al., 2002) and are in accord with estimated magmatic temperatures of the Bonin Ridge boninites (Umino et al., 2015).

Analyses of homogenised silicate MINCs project within the compositional array of major elements represented by the glasses, unhomogenised, glassy Cr-spinel-hosted MINCs and bulk rock data; the latter are regarded as defining a fractionation trend (e.g., Kanayama et al., 2012) Homogenised Cr-spinel-hosted MINCs have Cu contents below 10 ppm whereas even the most primitive, un-homogenised inclusions have at least 45 ppm Cu. This is highly unlikely to be the result of dilution of Cu during reverse crystallisation, as the degree of host or daughter mineral re-absorption would have to be on the order of 80% by volume. LA-ICP-MS scans across exposed, homogenised Cr-spinel-hosted MINCs reveal very different Cu distributions than equivalent, unhomogenised MINCs (Figure 8), which is a clear demonstration that Cu is mobile during heating. One possibility is that Cu is simply diffusing out of the melt inclusion during heating which has been observed in melt and fluid inclusions at much lower temperatures [Lerchbaumer and Audetat, 2012; Rottier et al., 2017]. A second possibility is the formation of sulfide at the edges of MINCs during heating or as a post entrapment process [Danyushevsky et al 2002], which would strongly partition Cu out of the silicate melt [Kamenetsky & Kamenetsky 2010].

Heating can also cause water loss from MINCs over very short time scales, especially at temperatures above 1200°C (Chen et al., 2011). Furthermore, the reappearance of shrinkage bubbles after quenching may be the result of plastic deformation of the host phases [Shiavi et al., 2016]. Both plastic deformation of the host crystals and water loss require serious consideration when heating MINCs to the temperatures needed to homogenise boninites [Danyushevsky et al., 2002; Chen et al., 2011; Shiavi et al., 2016]. As a consequence of these observations, analyses for

trace element and volatile abundance of homogenised MINCs was not pursued further. These samples have been used to demonstrate the effects of PEC on orthopyroxene-hosted MINCs however, as they reliably record major element compositions [Danyushevsky et al., 2002].

Major element compositions of orthopyroxene-hosted MINCs overlap with glasses and show excellent agreement, except for MgO and to a lesser degree, FeO (Figure 4). In fact, MgO contents of homogenised versus un-homogenised orthopyroxene-hosted MINCs are the most noticeable major element change observed consequent to heating experiments (Figure 9). Dissolution of the orthopyroxene host back into the MINC during heating is the most reasonable explanation to reconcile these observations. Clinopyroxene compositions, commonly crystallised in orthopyroxene-hosted MINCs, do not explain the differences in MgO contents between the homogenised and un-homogenised inclusions. Conversely, negligible PEC of Cr-spinel hosts is observed which is expected for minor phases such as Cr-spinel versus major phases like orthopyroxene (Kamenetsky, 1996). Daughter crystallisation of olivine and pyroxene in spinel-hosted MINCs and clinopyroxene in orthopyroxene-hosted MINCs is common. However, the compositional difference between host and daughter crystals makes them distinguishable under transmitted and reflected light as well as in BSE imagery (Figure 1) and therefore samples with significant daughter crystals can be avoided. When no daughter crystals are observed, the divergence of orthopyroxene-hosted MINC compositions away from the fractionation trend towards lower MgO concentrations is logically a result of host PEC, consistent with similar observations in olivine-hosted melt inclusions [Reference].

Melt inclusions that exhibit PEC of the host phase will have compositions out of equilibrium with those of the host. Partitioning of Mg and Fe between olivine and melt has been thoroughly characterised and used to recalculate MINC compositions (Roeder and Emslie, 1970; Kress and Ghiorso, 2004; Toplis 2005; Lloyd et al 2013; Wallace et al., 2015). The basic methodology involves adding equilibrium host back into the inclusion in small (0.1 wt. %) steps until the melt inclusion is in equilibrium with the entrapping host phase. Partitioning of Fe and Mg between orthopyroxene and

melt have also been measured experimentally (Beattie et al 1991; Waters and Lange, 2017) and similarly used to constrain post entrapment effects on orthopyroxene-hosted MINCs (Kress and Ghiorso, 2004). Partitioning of Fe and Mg between olivine and melt varies with SiO_2 and alkali contents of the melt and most of all, water content (Toplis, 2005). When olivine and orthopyroxene coexist in primitive boninites, partitioning of Mg and Fe between the two phases is shown to be co-dependant (Seckendorf and O'Neill, 1993). Furthermore, studies of orthopyroxene-rhyolite partitioning suggest variations with pressure, temperature and magmatic H_2O content, all significantly influence partitioning between orthopyroxene and melt (Waters and Lange, 2017). There is less parametrization of the effects of water content on Fe and Mg partitioning during orthopyroxene crystallisation versus olivine crystallisation. It is therefore difficult to evaluate the accuracy of any partition coefficient to reverse the effects of PEC in orthopyroxene-hosted, hydrous MINCs. Characterisation of the partitioning behaviour of Fe and Mg between crystal and melt does not include the presence of ferric iron in the melt. While ferric contents of olivine may be trivial (Canil and O'Neill, 1996), the same is not true for orthopyroxene (Canil and O'Neill, 1996; Malaspina et al 2012) and ferric contents of both crystal and melt should be accounted for when characterising Fe/Mg partitioning behaviour. Finally, the use of partition coefficients to 'reverse crystallise' PEC assumes the melt is in equilibrium with the host phase, and the partitioning behaviour remains constant during rapid crystallisation; the latter has been shown to vary significantly for olivine (Sossi and O'Neill 2016). However, to the authors' knowledge, there is no such information available for orthopyroxene. Published $^{Fe/Mg}K_D$ values for orthopyroxene and melt vary from 0.286 to 0.54 (Beattie et al 1991; Waters and Lange, 2017) due to factors discussed above and there does not appear to be any published values using melt compositions nearing boninitic. Calculations of the volume of PEC using this wide array of $^{Fe/Mg}K_D$ values produces estimates that vary by tens of percent. Other methods for estimating the extent of host PEC rely on distinguishing compositional differences between the original host and that which crystallised post entrapment (e.g. Lee and Stern, 1998).

However, backscatter FE-SEM imagery and high resolution EDS analyses show no compositional variation of host orthopyroxene proximal to MINCs.

With no suitable thermodynamic constraints to estimate the extent of post-entrapment crystallisation in orthopyroxene-hosted MINCs, the intercept of a melt inclusion-host tie line with the mean of the main fractionation trend has been used to estimate the original melt SiO_2 and MgO (Figure 10). This is similar to the approach of Watson (1976) wherein projections of tie lines between MINCs hosted in coexisting minerals were used to approximate the equilibrium melt composition common to all the host phases. It also assumes that the trends defined by glasses and Cr-spinel hosted melt inclusions are part of the same fractionating trends as the orthopyroxene-hosted MINCs Only values between 19-5 wt. % MgO were used here, which suit a linear fit. A 99 % confidence halo and a 95 % prediction interval were used to assess the level of uncertainty. The difference in MgO between the intercept and an analysed MINC composition is used to estimate the volume of host PEC. Natural compositional scatter of SiO_2 vs MgO yields a high level of uncertainty and glass compositions that overlap with orthopyroxene-hosted MINCs are given greater weight in interpretations. The orthopyroxene-hosted MINCs that lie within the 95 % prediction interval were used without recalculation to avoid adding further uncertainty. There is merit in trying to account for the PEC in orthopyroxene-hosted MINCs even though glass samples report most major and trace element concentrations, as glass has often lost volatiles, including H_2O, Cl and importantly S during eruption.

4.2 – A magnetite crisis, but the timing is different?

Rhyolite-MELTS simulations of boninite melt evolution via fractional crystallisation agrees well with the major element patterns defined by MINCs and glasses from the Bonin Ridge. The modelled timing of increased molar fraction of magnetite in the fractionating spinel phase paired with a sharp drop in melt fO_2 and a decrease in total iron suggests magnetite saturation occurred between 1-2 wt. % MgO. This matches the composition of glasses and melt inclusions that not only show a

matching decrease in FeO_T, but a drop in V, characteristic of magnetite saturation [Jenner et al., 2010]. A contemporaneous drop in Cu contents of boninite glasses and MINCs at 1-2 wt. % MgO suggests that sulfide saturation occurred at this point. Jenner et al., (2010; 2015) presented a well-constrained model termed "the magnetite crisis" of putative magnetite and sulfide saturation in EMBB and VFR melts, inferred from the geochemical composition of submarine-quenched glasses. However, no sulfide or magnetite was identified in support of the modelled trace element trends, and others have attributed the changes in chalcophile elements to their sequestration in and separation of a reduced, S-rich volatile phase [Sun et al., 2004]. The absence of magnetite or sulfide in the EMBB and VFR suites reported by Jenner et al (2010; 2015) renders resolution of this issue problematic. In the Bonin Ridge case, where the melts show remarkably similar patterns for Cu and V indicative of a magnetite crisis, sulfide and magnetite coincident with the inferred magnetite-triggered sulfide saturation are present (figure 11). This unequivocally links near-simultaneous magnetite and sulfide saturation to chalcophile trace element systematics for the first time. Timing of the appearance of magnetite and sulfide approximately match that of the modelled changes via Rhyolite-MELTS in FeO_T, as well as modelled timing of magnetite saturation and the necessary resultant drop in fO_2. The presence of sulfides strongly argues against the idea of volatile saturation as the prime mechanism leading to Cu depletion in the residual magma. Sulfide saturation occurs in evolved boninite series melts with crystal assemblages of Fe-rich orthopyroxene, clinopyroxene, magnetite and feldspar. The EMBB and SVFR melts experience magnetite and sulfide saturation at 3-4 wt. % MgO, while the Bonin Ridge melts were not saturated in magnetite and sulfide until 1-2 wt. % MgO. This apparent difference in the timing of sulfide saturation raises questions as to the controls on the timing of magnetite and sulfide saturation as discussed below. It is important firstly, to clearly define how relative timing or extent of magmatic evolution is expressed. The classic Harker diagram or bivariate plots with wt% MgO as the abscissa are commonly misinterpreted as directly and linearly reflecting extent of fractionation. A Daly gap where present for example, in specific volcanic suites has often been used to infer a paucity of magmas of intermediate SiO_2 composition

[Reubi & Blundy, 2009]. The alternative possibility of course is that variations in the nature of the solid fractionating assemblage results in strong variability in the rate of change of wt% SiO_2 (or MgO) with change in fraction of melt remaining (F) [Barclay & Carmichael, 2004].

Extensive orthopyroxene fractionation in Bonin Ridge boninites results in SiO_2 remaining essentially constant during periods of significant fractionation (Figure 5) due to the similarities in SiO_2 concentrations between melt and orthopyroxene. Therefore SiO_2 does not adequately define geochemical trends relative to degree of fractionation. This is analogous to the behaviour of SiO_2 in tholeiitic systems generally due to coprecipitation of clinopyroxene, plagioclase and olivine; a marked change in wt% MgO is adopted therein as the preferred plotting variable. Magmas with differences in the dominant fractionating phases will experience different rates of change in major element compositions relative to percent of fractionation. If the difference in composition of the primitive EMBB or SVFR and the boninites are considered in conjunction with the differences in major element composition of the dominant fractionating phases, (orthopyroxene versus clinopyroxene and plagioclase) relative timing becomes disguised. For example, 5% fractionation of orthopyroxene from primitive boninitic melt would reduce the melt MgO from 20% to 18.5% (-1.5%), while the same amount of fractionation of equal parts Pual Ridge clinopyroxene and plagioclase (Barriga et al., 2007) would reduce the MgO melt content by only 0.3%. Li et al., (2016) suggest an apparent rapid change in the rate of Cu enrichment in evolving arc melts coincident with the onset of plagioclase saturation: "we argue that plagioclase crystallisation is an important index for the enrichment of Cu during magma evolution, although the reasons behind this are not clear and need to be investigated further." It is of course clear that saturation of a melt with a MgO-deficient phase such as plagioclase results in a decrease in the rate of decline of wt% MgO as a function of F.

The extent of fractionation at the time of sulfide saturation was estimated for the boninite series melts as well as the EMBB and SVFR melts using K and Zr. Both elements are assumed to display

completely incompatible behaviour during Rayleigh fractionation and the degree of fractionation at the time of sulfide saturation was calculated in a standard way as:

$$C^i_{ss}/C^i_p = F^{(D-1)}$$

where C^i_{ss} = the concentration of element *i* at sulfide saturation, C^i_p = the concentration of element *i* in the parental melt, F = fraction of melt remaining, and D is the bulk distribution coefficient of element *i* (solid/liquid). D is assumed to be 0 and therefore the equation can be rewritten to estimate the percentage of fractional crystallisation when sulfide saturation occurs as follows.

$$\text{Percentage of crystallisation at sulfide saturation} = 100*[1-(1/(C_{ss}/C_p))]$$

This method yields an estimation of the degree of crystallisation of the boninite series melt at sulfide saturation of 56.7% and 56.2% for K and Zr respectively, which are close to the Rhyolite-MELTS estimate of 54.4 %. The same estimates were made using published values for K and Zr from the EMBB and SVFR (Jenner et al., 2010; 2015) yielding 72.8 % and 65.9 % respectively for the EMBB and 68.5 % and 62.5 % respectively for the SVFR. The most primitive compositions available (either from this study or literature values) are assumed to approximate parental melt composition of each melt. The dominant fractionating phases in the SVFR and EMBB melts are likely olivine, clinopyroxene and plagioclase (Li et al., 2016) while the dominant fractionating phase in the boninite series melts is likely orthopyroxene followed by clinopyroxene with olivine and spinel as volumetrically minor phases (Umino et al., 2015). Any compatibility of Zr or K into the fractionating phases would result in an underestimation of fractionation extent and is not thought to be significant in the boninite melts given the similarity of the Rhyolite-MELTS model and the K and Zr based estimations, while the same cannot be said for the EMBB or SVFR. Magma mixing is also not accounted for in these estimations, but is known to occur in boninite melts along the Bonin Ridge (Umino, 1986). Zirconium provides a lower estimate of fractionation than K in both EMBB and SVFR datasets as expected given the slight partitioning of K into plagioclase. Regardless, both estimates return higher degrees of fractionation in the EMBB and SVFR melts than in the boninites. Thus sulfide saturation occurred earlier in the

magmatic evolution of the boninite suites than either in the EMBB or SVFR melts, contrary to conclusions that might be drawn from the respective trends defined by MgO variations.

4.3 How is Sulfide Saturation Achieved?

Jenner et al. (2015) suggested that prior depletion of the mantle source of the EMBB melts resulted in low S abundances in the parental basalt magmas of the Basin and consequently retarded sulfide saturation. Jenner et al (2015) also noted the latter were more oxidised than the former, and that further oxidation during magmatic evolution stabilised sulphate, enabling a build-up of chalcophile elements prior to sulfide saturation (Jenner et al., 2010; 2015). The same logic was applied to the boninite series in this study, where depletion of the mantle source was assumed to be greater than that of the EMBB melts (Umino et al., 2015; 2018). In fact, sulfide saturation in the boninite series melts is somewhat surprising given the depleted mantle source from which they were generated and the incompatible nature of S during mantle melting (eg Fonseca et al., 2011; Lee et al., 2012). By 24% partial melting of the mantle, it is assumed that the entirety of base metal sulfides have been consumed (Luguet et al., 2007), leaving the mantle residue depleted in S and chalcophile elements. Indeed Cu and S contents of primitive boninite melts are approximately half those of the EMBB and SVFR melts. Sulfur concentrations of the EMBB melts were estimated using Se as a proxy, as S but not Se is variably degassed from the erupted glasses. Estimated S concentrations for EMBB melts prior to sulfide saturation are significantly above 500 ppm.

Modelling of boninite melt compositions at the time of sulfide saturation estimate a SCSS of 400-500 ppm (Fortin et al., 2015), however melt inclusion analyses show that S contents of boninite melts are low (figure 12) and do not approach estimates of SCSS. Although coverage of S contents across the melt compositions immediately prior to sulfide saturation are sparse, our petrographic studies nevertheless conclude that sulfide saturation was achieved.

There are several factors that could explain this discrepancy. First and foremost, melt inclusions may not reliably report S contents. Although S diffusion from melt inclusions is thought unlikely (Metrich

and Wallace, 2008), rapid post entrapment crystallisation can lead to vesiculation (Gerlach et al., 1996). Sulfur and CO_2 degassing has also been shown to occur in melt inclusions without significant PEC, where sulfide and carbonate minerals precipitate on shrinkage bubble walls [Kamenetsky and Kamenetsky 2010]. Kamenetsky and Kamenetsky (2010) argue that the demonstration of CO_2 and S degassing from melt inclusions can be used as an analogue for large scale magmatic processes. There are rare examples of sulfide and carbonate crystallisation on the walls of shrinkage bubbles in silicate melt inclusions from the Bonin Ridge, suggesting that both post-entrapment sulfur loss and (pre-entrapment) magmatic degassing of the boninite melts were possibilities. The latter offers a mechanism by which degassing magma could provide S to overlying melts; a mechanism which has been proposed to explain S enrichment in evolved porphyry-forming magmas (Hattori & Keith 2001; Wilkinson 2013; Henly et al., 2015; Blundy et al 2015).

In this study, only glassy melt inclusions with a single shrinkage bubble and no evidence of rapid PEC were analysed for S. Furthermore, selected shrinkage bubbles without evidence of crystallisation were analysed with RAMAN spectroscopy and returned spectra devoid of any volatile species. It is therefore considered unlikely that post-entrapment sulfur degassing occurred. Pre-eruptive magmatic degassing at such low S contents of these boninite melt inclusions is also unlikely considering that S will not saturate at such low concentrations (Mavrogenes and O'Neill 1999). However, S does partition readily into a co-existing volatile phase (Zajacz et al., 2015). Conventional wisdom suggests that a CO_2-rich gas phase will saturate at mid-crustal levels (Dixon and Stolper., 1995; Metrich and Wallace, 2008) into which S-species must partition to some extent. Primitive Bonin Ridge melts are reported to contain on the order of 50 ppm CO_2, and 2-5 wt.% H_2O (Umino et al., 2015). An evolving melt with these starting compositions would achieve volatile saturation at pressures above 1.5 kbar (Newman and Lowenstern 2002), indicating that pre-eruptive volatile degassing is a possibility. Sulfur dioxide has been shown to degas from magmas at higher pressures than Cl (Metrich and Wallace 2008; Lesne et al 2011). Bonin Ridge melt inclusions maintained constant S/Cl until sulfide saturation occurred, establishing sulfur loss was unlikely. Further,

predicted S content in the evolving Bonin Ridge magmas using Rhyolite-MELTS show S behaving incompatibly, with concentrations that agree with the melt inclusion analyses prior to sulfide saturation (Figure 12). An external source for S therefore requires consideration. Recharging of evolved boninite series melts with primitive boninite melts is known to occur along the Bonin Ridge (Umino, 1986). Considering the S contents measured in primitive Bonin Ridge melt inclusions are below 100 ppm it is unlikely that mixing of boninite series melts, primitive or evolved, would provide enough S to achieve sulfide saturation. Boninites along the Bonin Ridge are overlain by calcalkalic lavas sourced from more fertile mantle (Umino et al., 2015), but there is no evidence to support interaction between the 48-46 Ma boninites and the <45 Ma calcalkaline melts. Subsequent fertile arc-magma generation migrated away from the Mukojima and Chichijima Island groups (Kanayama et al., 2012). The lack of sulfur in evolving boninite series melts coupled with unequivocal evidence of sulfide saturation is puzzling.

Coincident timing of magnetite and sulfide saturation in the boninite series melts as indicated by geochemical trends and the appearance of magnetite and sulfide phases are echoed by trends defined in fractional crystallisation simulations using the Rhyolite-MELTS software. Estimations of $Fe^{3+}/\sum Fe$ using Xray Absorption Near Edge Spectroscopy (XANES) of boninite melt inclusions from the Bonin Islands and further north in the IBM system (Umino et al 2015; Brounce et al., 2015; Valetich et al in prep) suggest that even the primitive boninite melts are 1-2 $\log_{10}$ units above the fayalite – magnetite – quartz redox buffer, and favour the stabilisation of sulfate relative to sulfide (Jugo et al., 2010) especially at pressures significantly below 1.0 GPa. For sulfide to saturate under these conditions, the S-contents of the melt need to be much greater (Mavrogenes and O'Neill, 1999), such as those of the primitive Tolbachik melts, where at oxygen fugacities similar to the boninites, saturation in both sulfide and sulfate is achieved due to the presence of wt% levels of sulfur (Zelenski et al., 2018). Reduction of the boninite series melts due to magnetite crystallisation is therefore a likely control in the timing of sulfide saturation due to S concentrations being 2-3 orders of magnitude lower than the primitive Tolbachik melts. Experimental data suggests that the timing

of magnetite saturation is controlled in part by melt fO_2 (Berndt et al., 2004). Rhyolite-MELTS simulations of Bonin Ridge melt evolution show that the magnetite end-member of the fractionating spinel phase will dominate at a lower percent of melt fractionation when fO_2 is higher. Similarly, Petrolog3 simulations show that high fO_2 can trigger magnetite saturation at MgO > 8 wt. % in the EMBB and SVFR melts (Li et al., 2016). Another control on the timing of magnetite saturation is total iron content (FeO_T) of the melt, which is influenced by plagioclase fractionation, a major Fe-poor phase. Plagioclase saturation is repressed by high concentrations of H_2O in the melt (Arculus 2004) and is often the last major phase to appear in boninite melts, sometimes only appearing in the microcrystalline groundmass (Dobson et al., 2006). At the time of magnetite saturation, FeO_T was greater in both the EMBB and SVFR melts (Jenner et al., 2010; 2015) than in the boninite series melts. A combination of circumstances (melt composition, fractionation trends and fO_2) has been used to explain the ideal conditions for Cu enrichment in arc-related magmas from the Manus and Lau basins, while pressure and magmatic H_2O are considered weaker influences (Li et al., 2016). Oxygen fugacity sufficient to supress sulfide, but not too high as to trigger premature magnetite allows for the optimal Cu enrichment. If the FeO_T of the boninites is lower at the time of magnetite saturation compared to the EMBB and SVFR melts, then one possibility is that higher melt fO_2 in the boninite series melts resulted in an earlier magnetite crisis than in either the EMBB or SVFR melts.

4.4 Conclusions

A wide array of compositions, pressures and temperatures are observed in suprasubduction settings which generate a variable range of primary magmas collectively known as arc magmas. The association of arc magmatism with porphyry-epithermal mineralisation is a strong motivation to investigate metal behaviour in these complex systems. Previous work on the Manus and Lau basins highlights how variations in the timing of sulfide and volatile saturation can dramatically influence the behaviour of metals in evolving arc melts. Presented here is a contribution to the understanding of chalcophile evolution in boninite melts from their type locality, the Bonin Ridge. Boninites are a

particularly distinctive arc magma type (cf Golowin et al., 2017) due to the conditions under which these melts are produced from depleted mantle sources, making them a valuable case study for the relative controls of composition and magmatic evolution on the behaviour of chalcophile elements. Very similar trace element patterns to those of the EMBB and SVFR are found in the boninite series melts indicate magnetite-triggered-sulfide-saturation has occurred. Furthermore, we have identified the first physical evidence of coexisting sulfide and magnetite to explain the geochemical trends, refuting suggestions that changes in Cu are due to S-rich devolatilisation. It is further demonstrated that sulfide saturation occurred in the boninite melts after a lower degree of fractionation than either the EMBB or SVFR melts. A higher fO_2 in the evolved boninites relative to either the SVFR or EMBB explains the timing of magnetite saturation. This is counterintuitive when relating magmatic geochemical trends to the concentrations of MgO or SiO_2 as is usually the practice, but relative enrichments of incompatible minor and trace elements suggests that MgO is not necessarily a useful proxy for comparing the relative degrees of melt fractionation between different magma types. Given the extent of prior melt extraction of the mantle sources for boninites (up to 30%) coupled with the incompatible nature of S during mantle melting, it is surprising that sulfide saturation is achieved at all during the evolution of the boninite series melts. Nevertheless, we have documented examples of silicate and sulfide inclusions coexisting in the same host crystal, and silicate melt inclusions with daughter crystals of both magnetite and sulfide. The apparent lack of sulfur in boninite melt inclusions compounds the unanswered problem of how sulfide saturation was achieved.

Acknowledgements

This research benefitted from funding from the Australian Research Council as well as the Australian and New Zealand International Ocean Discovery Program (International Ocean Discovery Program). Support to attend ECROFI 2017 was provided by the Society of Geology Applied to Mineral Deposits (SGA). The authors are thankful to Frank Brink, Hua Chen and Jeff Chang from the Centre of

Advanced Microscopy at The Australian National University, for assistance with FE-SEM imaging as well as quantitative EDS and EPMA analyses. Finally, the authors owe thanks to Paul Wallace and two anonymous reviewers for incredibly constructive feedback regarding this manuscript.

Anenburg, M. and J. A. Mavrogenes (2016). "Experimental observations on noble metal nanonuggets and Fe-Ti oxides, and the transport of platinum group elements in silicate melts." Geochimica et Cosmochimica Acta 192: 258-278.

Arculus, R. J. (2004). "Evolution of arc magmas and their volatiles." The State of the Planet: Frontiers and Challenges in Geophysics: 95-108.

Arculus, R. J., et al. (2015). "A record of spontaneous subduction initiation in the Izu-Bonin-Mariana arc." Nature Geoscience 8(9): 728-733.

Arculus, R. J. and R. Powell (1986). "Source component mixing in the regions of arc magma generation." Journal of Geophysical Research: Solid Earth 91(B6): 5913-5926.

Barclay, J. and I. Carmichael (2004). "A hornblende basalt from western Mexico: water-saturated phase relations constrain a pressure–temperature window of eruptibility." Journal of Petrology 45(3): 485-506.

Barriga, F., et al. (2007). "1. Leg 193 Synthesis: Anatomy of an active felsic-hosted hydrothermal system, eastern Manus Basin, Papua New Guinea."

Beattie, P., et al. (1991). "Partition coefficients for olivine-melt and orthopyroxene-melt systems." Contributions to Mineralogy and Petrology 109(2): 212-224.

Berndt, J., et al. (2004). "An experimental investigation of the influence of water and oxygen fugacity on differentiation of MORB at 200 MPa." Journal of Petrology 46(1): 135-167.

Blundy, J., et al. (2015). "Generation of porphyry copper deposits by gas-brine reaction in volcanic arcs." Nature Geoscience 8(3): 235-240.

Brounce, M., et al. (2015). "Temporal evolution of mantle wedge oxygen fugacity during subduction initiation." Geology 43(9): 775-778.

Bryant, C., et al. (2003). "The geochemical evolution of the Izu-Bonin arc system: A perspective from tephras recovered by deep-sea drilling." Geochemistry, Geophysics, Geosystems 4(11).

Burnham, C. W. (1994). "Development of the Burnham model for prediction of H 2 O solubility in magmas." Reviews in Mineralogy and Geochemistry 30(1): 123-129.

Cameron, W. (1985). "Petrology and origin of primitive lavas from the Troodos ophiolite, Cyprus." Contributions to Mineralogy and Petrology 89(2-3): 239-255.

Cameron, W., et al. (1983). "Boninite petrogenesis: chemical and Nd-Sr isotopic constraints." Earth and Planetary Science Letters 65(1): 75-89.

Canil, D. and H. S. C. O'Neill (1996). "Distribution of ferric iron in some upper-mantle assemblages." Journal of Petrology 37(3): 609-635.

Chen, Y., et al. (2011). "The rate of water loss from olivine-hosted melt inclusions." Contributions to Mineralogy and Petrology 162(3): 625-636.

Crawford, A. J., et al. (1989). "Classification, petrogenesis and tectonic setting of boninites."

Danyushevsky, L., et al. (2000). "Re-equilibration of melt inclusions trapped by magnesian olivine phenocrysts from subduction-related magmas: petrological implications." Contributions to Mineralogy and Petrology 138(1): 68-83.

Danyushevsky, L. V., et al. (2002). "Experimental and petrological studies of melt inclusions in phenocrysts from mantle-derived magmas: an overview of techniques, advantages and complications." Chemical Geology 183(1): 5-24.

Dixon, J. E. and E. M. Stolper (1995). "An experimental study of water and carbon dioxide solubilities in mid-ocean ridge basaltic liquids. Part II: applications to degassing." Journal of Petrology 36(6): 1633-1646.

Dobson, P. F., et al. (2006). "Petrology and geochemistry of boninite-series volcanic rocks, Chichi-Jima, Bonin Islands, Japan." International Geology Review 48(8): 669-701.

Falloon, T. J. and L. V. Danyushevsky (2000). "Melting of refractory mantle at 1· 5, 2 and 2· 5 GPa under anhydrous and H2O-undersaturated conditions: implications for the petrogenesis of high-Ca boninites and the influence of subduction components on mantle melting." Journal of Petrology 41(2): 257-283.

Falloon, T. J., et al. (2008). "Boninites and adakites from the northern termination of the Tonga Trench: implications for adakite petrogenesis." Journal of Petrology 49(4): 697-715.

Fellows, S. A. and D. Canil (2012). "Experimental study of the partitioning of Cu during partial melting of Earth's mantle." Earth and Planetary Science Letters 337: 133-143.

Fonseca, R. O., et al. (2011). "Solubility of Os and Ir in sulfide melt: Implications for Re/Os fractionation during mantle melting." Earth and Planetary Science Letters 311(3-4): 339-350.

Fortin, M.-A., et al. (2015). "The effect of water on the sulfur concentration at sulfide saturation (SCSS) in natural melts." Geochimica et Cosmochimica Acta 160: 100-116.

Gaetani, G. A. and E. B. Watson (2000). "Open system behavior of olivine-hosted melt inclusions." Earth and Planetary Science Letters 183(1): 27-41.

Gerlach, T. M., et al. (1996). "Preeruption vapor in magma of the climactic Mount Pinatubo eruption: Source of the giant stratospheric sulfur dioxide cloud." Fire and mud: eruptions and lahars of Mount Pinatubo, Philippines 415: 33.

Golowin, R., et al. (2017). "Boninite-like intraplate magmas from Manihiki Plateau require ultra-depleted and enriched source components." Nature communications 8: 14322.

Gualda, G. A., et al. (2012). "Rhyolite-MELTS: a modified calibration of MELTS optimized for silica-rich, fluid-bearing magmatic systems." Journal of Petrology 53(5): 875-890.

Hattori, K. H. and J. D. Keith (2001). "Contribution of mafic melt to porphyry copper mineralization: evidence from Mount Pinatubo, Philippines, and Bingham Canyon, Utah, USA." Mineralium Deposita 36(8): 799-806.

Hedenquist, J. W. and J. B. Lowenstern (1994). "The role of magmas in the formation of hydrothermal ore deposits." Nature 370(6490): 519-527.

Henley, R. W., et al. (2015). "Porphyry copper deposit formation by sub-volcanic sulphur dioxide flux and chemisorption." Nature Geoscience 8(3): 210-215.

Hunt, J. (1977). "Porphyry copper deposits." Geological Society, London, Special Publications 7(1): 98-98.

Ishizuka, O., et al. (2006). "Early stages in the evolution of Izu–Bonin arc volcanism: New age, chemical, and isotopic constraints." Earth and Planetary Science Letters 250(1): 385-401.

Ishizuka, O., et al. (2011). "The timescales of subduction initiation and subsequent evolution of an oceanic island arc." Earth and Planetary Science Letters 306(3): 229-240.

Jenner, F., et al. (2012). "Chalcophile element systematics in volcanic glasses from the northwestern Lau Basin." Geochemistry, Geophysics, Geosystems 13(6).

Jenner, F. E., et al. (2015). "The competing effects of sulfide saturation versus degassing on the behavior of the chalcophile elements during the differentiation of hydrous melts." Geochemistry, Geophysics, Geosystems 16(5): 1490-1507.

Jenner, F. E., et al. (2009). "Determination of Selenium Concentrations in NIST SRM 610, 612, 614 and Geological Glass Reference Materials Using the Electron Probe, LA-ICP-MS and SHRIMP II." Geostandards and Geoanalytical Research 33(3): 309-317.

Jenner, F. E., et al. (2010). "The magnetite crisis in the evolution of arc-related magmas and the initial concentration of Au, Ag and Cu." Journal of Petrology 51(12): 2445-2464.

Jenner, F. E. and H. S. C. O'Neill (2012). "Analysis of 60 elements in 616 ocean floor basaltic glasses." Geochemistry, Geophysics, Geosystems 13(2).

Jochum, K. P., et al. (2011). "Determination of reference values for NIST SRM 610–617 glasses following ISO guidelines." Geostandards and Geoanalytical Research 35(4): 397-429.

Jugo, P. J., et al. (2010). "Sulfur K-edge XANES analysis of natural and synthetic basaltic glasses: Implications for S speciation and S content as function of oxygen fugacity." Geochimica et Cosmochimica Acta 74(20): 5926-5938.

Kamenetsky, V. (1996). "Methodology for the study of melt inclusions in Cr-spinel, and implications for parental melts of MORB from FAMOUS area." Earth and Planetary Science Letters 142(3-4): 479-486.

Kamenetsky, V. S., et al. (2001). "Factors controlling chemistry of magmatic spinel: an empirical study of associated olivine, Cr-spinel and melt inclusions from primitive rocks." Journal of Petrology 42(4): 655-671.

Kamenetsky, V. S. and M. B. Kamenetsky (2010). "Magmatic fluids immiscible with silicate melts: examples from inclusions in phenocrysts and glasses, and implications for magma evolution and metal transport." Geofluids 10(1-2): 293-311.

Kanayama, K., et al. (2012). "Eocene volcanism during the incipient stage of Izu–Ogasawara Arc: Geology and petrology of the Mukojima Island Group, the Ogasawara Islands." Island Arc 21(4): 288-316.

König, S., et al. (2010). "Boninites as windows into trace element mobility in subduction zones." Geochimica et Cosmochimica Acta 74(2): 684-704.

Kress, V. C. and M. S. Ghiorso (2004). "Thermodynamic modelling of post-entrapment crystallization in igneous phases." Journal of Volcanology and Geothermal Research 137(4): 247-260.

Le Bas, M. (2000). "IUGS reclassification of the high-Mg and picritic volcanic rocks." Journal of Petrology 41(10): 1467-1470.

Lee, C.-T. A., et al. (2012). "Copper systematics in arc magmas and implications for crust-mantle differentiation." Science 336(6077): 64-68.

Lee, J. and R. J. Stern (1998). "Glass inclusions in Mariana arc phenocrysts: A new perspective on magmatic evolution in a typical intra-oceanic arc." The Journal of Geology 106(1): 19-34.

Lerchbaumer, L. and A. Audétat (2012). "High Cu concentrations in vapor-type fluid inclusions: An artifact?" Geochimica et Cosmochimica Acta 88: 255-274.

Lesne, P., et al. (2011). "Experimental simulation of closed-system degassing in the system basalt–H2O–CO2–S–Cl." Journal of Petrology 52(9): 1737-1762.

Li, J.-X., et al. (2011). "Post-collisional ore-bearing adakitic porphyries from Gangdese porphyry copper belt, southern Tibet: melting of thickened juvenile arc lower crust." Lithos 126(3): 265-277.

Li, Z.-G., et al. (2016). "Origin of selective enrichment of Cu and Au in sulfide deposits formed at immature back-arc ridges: Examples from the Lau and Manus basins." Ore Geology Reviews 74: 52-62.

Lloyd, A. S., et al. (2013). "Volatile loss from melt inclusions in pyroclasts of differing sizes." Contributions to Mineralogy and Petrology 165(1): 129-153.

Lowell, J. D. and J. M. Guilbert (1970). "Lateral and vertical alteration-mineralization zoning in porphyry ore deposits." Economic Geology 65(4): 373-408.

Luguet, A., et al. (2007). "Residual platinum-group minerals from highly depleted harzburgites of the Lherz massif (France) and their role in HSE fractionation of the mantle." Geochimica et Cosmochimica Acta 71(12): 3082-3097.

Malaspina, N., et al. (2012). "Fe3+ distribution between garnet and pyroxenes in mantle wedge carbonate-bearing garnet peridotites (Sulu, China) and implications for their oxidation state." Lithos 146: 11-17.

Massare, D., et al. (2002). "High-temperature experiments on silicate melt inclusions in olivine at 1 atm: inference on temperatures of homogenization and H 2 O concentrations." Chemical Geology 183(1): 87-98.

Mavrogenes, J. and J. Blundy (2017). "Crustal sequestration of magmatic sulfur dioxide." Geology 45(3): 211-214.

Mavrogenes, J. A. and H. S. C. O'Neill (1999). "The relative effects of pressure, temperature and oxygen fugacity on the solubility of sulfide in mafic magmas." Geochimica et Cosmochimica Acta 63(7-8): 1173-1180.

McDonough, W. F. and S.-S. Sun (1995). "The composition of the Earth." Chemical Geology 120(3-4): 223-253.

Métrich, N. and P. J. Wallace (2008). "Volatile abundances in basaltic magmas and their degassing paths tracked by melt inclusions." Reviews in Mineralogy and Geochemistry 69(1): 363-402.

Mungall, J. E. (2002). "Roasting the mantle: Slab melting and the genesis of major Au and Au-rich Cu deposits." Geology 30(10): 915-918.

Newman, S. and J. B. Lowenstern (2002). "VolatileCalc: a silicate melt–H2O–CO2 solution model written in Visual Basic for excel." Computers & Geosciences 28(5): 597-604.

Park, J.-W., et al. (2015). "The role of late sulfide saturation in the formation of a Cu-and Au-rich magma: Insights from the platinum group element geochemistry of Niuatahi–Motutahi lavas, Tonga rear arc." Journal of Petrology 56(1): 59-81.

Parkinson, I. J. and J. A. Pearce (1998). "Peridotites from the Izu–Bonin–Mariana forearc (ODP Leg 125): evidence for mantle melting and melt–mantle interaction in a supra-subduction zone setting." Journal of Petrology 39(9): 1577-1618.

Pearce, J. A. and I. J. Parkinson (1993). "Trace element models for mantle melting: application to volcanic arc petrogenesis." Geological Society, London, Special Publications 76(1): 373-403.

Reagan, M. K., et al. (2010). "Fore-arc basalts and subduction initiation in the Izu-Bonin-Mariana system." Geochemistry, Geophysics, Geosystems 11(3).

Reagan, M. K., et al. (2017). "Subduction initiation and ophiolite crust: new insights from IODP drilling." International Geology Review: 1-12.

Reubi, O. and J. Blundy (2009). "A dearth of intermediate melts at subduction zone volcanoes and the petrogenesis of arc andesites." Nature 461(7268): 1269.

Richards, J. (2003). "Tectono-magmatic precursors for porphyry Cu-(Mo-Au) deposit formation." Economic Geology 98(8): 1515-1533.

Roeder, P. and R. Emslie (1970). "Olivine-liquid equilibrium." Contributions to Mineralogy and Petrology 29(4): 275-289.

Rottier, B., et al. (2017). "Trace element diffusion and incorporation in quartz during heating experiments." Contributions to Mineralogy and Petrology 172(4): 23.

Schiavi, F., et al. (2016). "P–V–T–X evolution of olivine-hosted melt inclusions during high-temperature homogenization treatment." Geochimica et Cosmochimica Acta 172: 1-21.

Schmidt, M. and O. Jagoutz (2017). "The global systematics of primitive arc melts." Geochemistry, Geophysics, Geosystems.

Sillitoe, R. H. (2010). "Porphyry copper systems." Economic Geology 105(1): 3-41.

Sossi, P. A. and H. S. C. O'Neill (2016). "Liquidus temperatures of komatiites and the effect of cooling rate on element partitioning between olivine and komatiitic melt." Contributions to Mineralogy and Petrology 171(5): 49.

Stern, R. J., et al. (1991). "The source of the subduction component in convergent margin magmas: trace element and radiogenic isotope evidence from Eocene boninites, Mariana forearc." Geochimica et Cosmochimica Acta 55(5): 1467-1481.

Sun, W., et al. (2003). "Evidence for rhenium enrichment in the mantle wedge from submarine arc–like volcanic glasses (Papua New Guinea)." Geology 31(10): 845-848.

Sun, W., et al. (2004). "Release of gold-bearing fluids in convergent margin magmas prompted by magnetite crystallization." Nature 431(7011): 975-978.

Sun, W., et al. (2011). "The genetic association of adakites and Cu–Au ore deposits." International Geology Review 53(5-6): 691-703.

Toplis, M. (2005). "The thermodynamics of iron and magnesium partitioning between olivine and liquid: criteria for assessing and predicting equilibrium in natural and experimental systems." Contributions to Mineralogy and Petrology 149(1): 22-39.

Umino, S. (1985). "Volcanic geology of Chichijima, the Bonin Islands (Ogasawara Islands)." J. Geol. Soc. Jpn 91: 505-523.

Umino, S. (1986). "Magma mixing in boninite sequence of Chichijima, Bonin Islands." Journal of Volcanology and Geothermal Research 29(1-4): 125-157.

Umino, S., et al. (2018). "Did boninite originate from the heterogeneous mantle with recycled ancient slab?" Island Arc.

Umino, S., et al. (2015). "Thermal and chemical evolution of the subarc mantle revealed by spinel-hosted melt inclusions in boninite from the Ogasawara (Bonin) Archipelago, Japan." Geology 43(2): 151-154.

von Seckendorff, V. and H. S. C. O'Neill (1993). "An experimental study of Fe-Mg partitioning between olivine and orthopyroxene at 1173, 1273 and 1423 K and 1.6 GPa." Contributions to Mineralogy and Petrology 113(2): 196-207.

von Seckendorff, V. and H. S. C. O'Neill (1993). "An experimental study of Fe-Mg partitioning between olivine and orthopyroxene at 1173, 1273 and 1423 K and 1.6 GPa." Contributions to Mineralogy and Petrology 113(2): 196-207.

Wallace, P. J. (2005). "Volatiles in subduction zone magmas: concentrations and fluxes based on melt inclusion and volcanic gas data." Journal of Volcanology and Geothermal Research 140(1): 217-240.

Wallace, P. J., et al. (2015). "Melt inclusion CO2 contents, pressures of olivine crystallization, and the problem of shrinkage bubbles." American Mineralogist 100(4): 787-794.

Wang, Z. and H. Becker (2015). "Abundances of Ag and Cu in mantle peridotites and the implications for the behavior of chalcophile elements in the mantle." Geochimica et Cosmochimica Acta 160: 209-226.

Waters, L. E. and R. A. Lange (2017). "An experimental study of $^{Fe2+}$ - $^{Mg}K_D$ between orthopyroxene and rhyolite: a strong dependence on H2O in the melt." Contributions to Mineralogy and Petrology 172(6): 42.

Watson, E. B. (1976). "Glass inclusions as samples of early magmatic liquid: determinative method and application to a South Atlantic basalt." Journal of Volcanology and Geothermal Research 1(1): 73-84.

Wilkinson, J. J. (2013). "Triggers for the formation of porphyry ore deposits in magmatic arcs." Nature Geoscience 6(11): 917-925.

Zajacz, Z. (2015). "The effect of melt composition on the partitioning of oxidized sulfur between silicate melts and magmatic volatiles." Geochimica et Cosmochimica Acta 158: 223-244.

Zelenski, M., et al. (2018). "Silicate-sulfide liquid immiscibility in modern arc basalt (Tolbachik volcano, Kamchatka): Part I. Occurrence and compositions of sulfide melts." Chemical Geology 478: 102-111.

Table and figure captions

Table 1

Representative analyses from melt inclusions and glasses from the Bonin Ridge. Average values are provided for NIST SRM612 during LA-ICP-MS analyses. RSD (Relative Standard Deviation). These values are compared to the GeoReM range (Jochum, 2011) as well as the preferred values of Jenner et al., (2010). The entire set of analyses can be found in supplementary tables T1 and T2 for major and trace element analyses respectively.

Table 2

Cr-spinel hosted melt inclusion with primitive boninitic composition compared to the starting composition used in Rhyolite-MELTS for fractional crystallisation simulations. Starting melt conditions used in the simulation are included.

Figure Captions

Description: Photo plate of various melt inclusions. This is a 2 - column figure. CAPTION:

Figure 1. Melt inclusions (MINCs) hosted in various phases. **A-D – MINCs hosted in Cr-spinel**. A). Reflected light micrograph of pristine tetragonal inclusion with exposed bubble cast. B). Scanning

electron image of pristine MINC and exposed bubble cast. D). C). Largely glassy MINC with feathery pyroxene crystallised on the inclusion walls and exposed bubble cast D). MINC with radiating and interlocked quench crystals, and elongate bubbles with only interstitial glass remaining. **E-H – orthopyroxene-hosted MINCs.** E). Transmitted light micrograph of homogeneously trapped MINCS with consistent shrinkage bubbles and no visible PEC. Transmitted light micrograph of partially exposed MINC with shrinkage bubble still buried and minor PEC on MINC wall. G). Reflected and transmitted light micrographs of MINC with significant PEC of clinopyroxene along the inclusion rim. H). Transmitted light micrograph of homogeneously trapped melt inclusions with extensive PEC. **I-L magnetite-hosted MINCs** I).Reflected light micrograph of a magnetite inclusion in a pyroxene crystal. The magnetite has a large, pristine melt inclusion with a buried shrinkage bubble. J). MINC with extensive PEC of clinopyroxene and several shrinkage bubble. Small round sulfides are present in the remaining silicate glass K). BSE image of pristine magnetite-hosted MINC. L) BSE image of magnetite hosted melt inclusions, showing skeletal daughter phases formed during quench.

Figure 2

Description: 2 column figure.

Figure 2. Orthopyroxene crystals showing; A) Heterogeneous trapping of Silicate (Si)-melt, magnetite (Mt), plagioclase microcrysts and sulfide. The variable proportions of plagioclase to melt suggests trapping of existing crystals as opposed to PEC. B) Homogenous trapping of silicate melt inclusions with PEC of magnetite and plagioclase. All inclusions have proportionally consistent bubbles (Bbl) and magnetite daughter crystals.

Figure 3

Description: 1 column Figure

Figure 3. A). Transmitted light micrograph of orthopyroxene-hosted melt inclusions with proportionally equal amounts of crystallisation suggesting it occurred post entrapment. B). Reflected

light micrograph of same large MINC displayed in A) showing variable morphologies of sulfide saturation. Pure sulfide droplets are present in the remaining glass and are also trapped in silicate PEC (C and E respectively). Other sulfides with a crystalline appearance can be seen in on the surface of magnetite PEC (D)

Figure 4

Description: This is a 2 column figure

Figure 4. A). MgO vs SiO2 showing the fractionation trend from primitive (high MgO, low SiO2) to evolved (low MgO, high SiO2) Boninite series compositions. The effects of host PEC on orthopyroxene-hosted MINCs are highlighted in brown. B-E). MgO versus CaO, Al_2O_3, FeO_T and K_2O respectively. The Rhyolite-MELTS model (red line) in each plot agrees well with the data.

Figure 5

Description: this is a 2-column figure

Figure 5. Rhyolite-MELTS model showing degree of fractional crystallisation (1-F) versus SiO_2 and MgO respectively with dominant fractionating phases labelled. When orthopyroxene is the dominant fractionating phase, SiO_2 changes very little.

Figure 6

Description: 1.5 - column figure.

Figure 6. Primitive upper mantle-normalised trace element patterns (A) and chondrite normalised REE patterns (B) showing representative glass compositions from Mukojma and Chichijima as well as orthopyroxene-hosted and Cr-spinel-hosted MINCs. Normalising factors after Pearce and Parkinson, (1993) and McDonough and Sun, (1995) respectively.

Figure 7

Description: 2 Column figure

Figure 7. MgO and K_2O versus Cu, V, Zn and Sc. Blue and Red zones mark the timing of magnetite triggered sulfide saturation for the Bonin Ridge melts and the EMBB and VFR melts respectively. Cu and V both show changes in abundance <2 wt. % MgO and at approximately 0.6 wt. % K_2O. Data for MORB (Jenner and O'Neill, 2012). Data for EMBB (Jenner et al., 2010). Data for SVFR (Jenner et al., 2015).

Figure 8

Description: 1 Column figure

Figure 8. LA-ICP-MS Traverses over A) A homogenised Cr-spinel hosted melt inclusion which has been rapidly heated to 1350^{o}C and held at temperature for 5 minutes and before quenching in water versus B) An unhomogenised Cr-spinel hosted melt inclusion. Y-axis is raw LA-ICP-MS data used to display the distribution of Cu between homogenised and unhomogenised MINCS

Figure 9

Description 1.5 Column Figure

Figure 9. MgO vs SiO_2 displaying the main fractionation trend of spinel- and orthopyroxene-hosted MINCs and glasses. An orthopyroxene host and MINC pair shown as solid red squares are joined by a dashed line. The homogenised orthopyroxene-hosted MINCs show higher MgO at a given SiO_2 than unhomogenised orthopyroxene-hosted MINCs consistent with mixing between unhomogenised orthopyroxene-hosted MINCs and their hosts

Figure 10

Description: 1 column Figure

Figure 10 A). MgO vs SiO_2 plot with an example of the estimation of post entrapment crystallisation in an orthopyroxene-hosted MINC. The intercept of the host-inclusion mixing line with the mean of the main fractionation trend is used to estimate the volume of PEC. B) MgO vs SiO_2 plot showing the

mean of the fractionation trend and the confidence interval (red dashed lines) showing the 99% probability of the position of the mean. The prediction interval (green dashed lines) is the 2 standard deviation spread on the main fractionation trend. If the orthopyroxene-hosted melt inclusions lie within the green dashed lines, they are used without recalculation, to avoid adding unnecessary uncertainty

Figure 11

Description: This is a 2 Column figure

Figure 11. Reflected light micrographs showing various entrapment textures for sulfides and magnetite. From top left going clockwise; 1) Fe-Ni-sulfides in contact with magnetite (Mt) and plagioclase (Plag) phenocysts in a melt enclave (Si-melt); 2) Cu-rich sulfide inclusion in magnetite host. Exsolution textures suggests the sulfide was trapped as melt; 3) Sulfide and silicate melt inclusions within a magnetite host, which itself is trapped in a clinopyroxene (Cpx) phenocryst. 4). Silicate melt trapped with magnetite and Fe-sulfide. Note, the magnetite inclusion has a small sulfide inclusion of its own. 5) Fe-Cu-sulfide trapped with a small amount of silicate melt and a plagioclase crystal. 6). Silicate melt inclusion hosted in orthopyroxene (Opx) with small magnetite and sulfide grains.

Figure 12

Description: 1 column figure

Figure 12. MgO versus S and Cl/S in melt inclusions. Blue zone shows the timing of sulfide saturation and red line shows the behaviour of S modelled in Rhyolite-MELTS. Cl/S remains constant prior to sulfide saturation, after which S concentration in the melt decreases while Cl continues to increase.

Table 1: Major and trace element analyses of representative MINC and glass samples from the Bonin Islands

Host	Cr-Spinel		Glass		Orthopyroxene		Magnetite	**NIST SRM 612**				
								Average	RSD (%)	n=	GeoReM	Jenner, 2010
wt. %												
SiO_2	54.98	57.33	58.89	63.29	58.00	59.50	74.60					
Al_2O_3	6.97	7.53	10.31	14.39	8.72	10.17	12.90					
FeO_T	8.54	8.68	9.00	6.81	9.75	9.17	2.20					
MgO	18.35	15.04	8.55	1.21	7.67	5.77	bdl					
CaO	5.47	5.48	8.24	6.02	7.89	8.70	2.44					
Na_2O	1.13	1.16	1.66	2.25	1.48	1.60	2.62					
K_2O	0.33	0.35	0.42	0.60	0.35	0.40	0.82					
TiO_2	0.04	0.01	0.07	0.07	0.14	0.10	0.08					
P_2O_5	0.01	0.00	0.02	0.05	0.04	0.06	bdl					
MnO	0.06	0.05	0.18	0.03	0.22	0.13	bdl					
Cr_2O_3	0.46	0.29	0.06	0.01	0.05	0.03	bdl					
Total	96.39	95.96	97.41	94.79	94.35	95.72	95.64					
ppm												
Cl	313	381	414	801	402	600						
Sc	29.5	34.9	40.6	18.4	44.9	39.7	8.8	40.6	2.4	22	39.9	39.0
Ti	391.5	452.1	614.6	775.2				40.4	2.2	24	44.0	41.0
V	147.7	189.7	206.1	173.0	215.8	210.6	1.0	38.7	1.9	22	38.8	39.0
Cr	788.2	420.5	410.7	2.2	330.8	193.2	bdl	36.3	1.5	22	36.4	39.9
Mn	60.3		1312.4	800.2				38.5	0.4	8	38.7	38.0
Co		47.4	42.5	17.9	41.8	33.9		35.0	0.5	17	35.5	35.0
Ni	301.5	62.4	60.6	1.1	30.6	16.6		38.9	0.9	20	38.8	38.8
Cu	51.7	73.0	76.5	105.8	79.2	78.6	19.0	40.1	1.7	22	37.8	37.0
Zn	74.5	83.4	80.2	79.9	88.0	79.5		37.9	4.3	18	39.1	38.0

(continued)

Table 1: Continued

Host	Cr-Spinel		Glass		Orthopyroxene		Magnetite	**NIST SRM 612**				
								Average	RSD (%)	n=	GeoReM	Jenner, 2010
Rb			12.3	19.8				31.8	0.5	4	31.4	31.4
Sr			83.1	134.0				79.1	0.4	4	78.4	78.4
Y			3.6	4.3				38.9	1.3	8	38.3	38.0
Zr			18.3	26.8			34.9	38.7	1.4	12	37.9	38.0
Nb			0.4	0.6			0.2	39.0	1.1	7	38.9	40.0
Ba			40.9	69.4				39.1	0.7	4	39.3	39.7
La			0.9	1.4				36.0	1.4	7	36.0	35.8
Ce			1.8	2.7			4.7	39.0	1.6	9	38.4	38.7
Pr			0.3	0.4				38.0	0.6	4	37.9	39.0
Nd			1.3	1.8			3.0	35.8	1.5	7	35.5	35.9
Sm			0.3	0.5				37.9	0.3	4	37.7	38.1
Eu			0.1	0.2			0.3	36.1	1.1	7	35.6	35.0
Gd			0.5	0.5			1.0	37.9	3.1	7	37.3	36.7
Tb			0.1	0.1				37.2	0.5	7	37.6	38.3
Dy			0.6	0.7				35.9	0.3	4	35.5	36.0
Ho			0.1	0.1				38.2	0.4	5	38.3	38.0
Er			0.4	0.5				38.5	0.4	5	38.0	38.0
Tm			0.1	0.1				37.1	0.3	5	36.8	38.0
Yb			0.5	0.6			1.2	37.8	3.8	8	39.2	37.1
Lu			0.1	0.1				36.9	0.5	5	37.0	37.2
Hf			0.5	0.8				37.3	1.0	4	36.7	37.9
Pb	1.1	1.7	1.7	2.8	1.4	1.9	3.0	38.1	1.4	21	38.6	38.6
Th			0.1	0.2			0.3	37.9	2.2	6	37.8	37.8
U			0.1	0.2			0.2	37.3	2.6	6	37.4	37.4

Table 2: Primitive boninite composition vs Rhyolite-MELTS starting composition and conditions

	Cr-spinel hosted melt inclusion	Rhyolite-MELTS starting composition
wt. %		
SiO_2	54.98	54.73
Al_2O_3	6.97	6.94
FeO_T	8.54	8.50
MgO	18.35	18.27
CaO	5.47	5.44
Na_2O	1.13	1.12
K_2O	0.33	0.33
TiO_2	0.04	0.04
P_2O_5	0.01	0.01
MnO	0.06	0.00
Cr_2O_3	0.46	0.46
H_2O	-	3.98
S (ppm)	40	80
fO_2 (ΔQFM)	-	1.04
Temperature (T °C)	-	1424
Pressure (P bar)	-	5600
dP/dT (bar/°C)	-	9

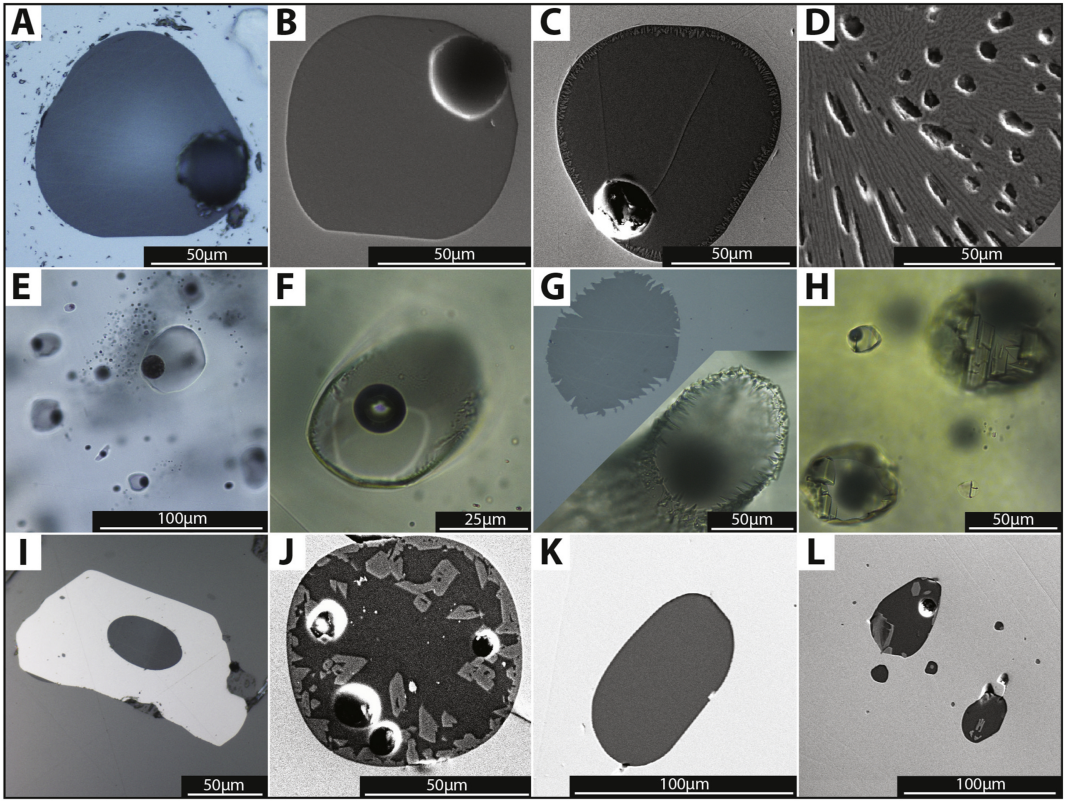
A
50µm
B
50µm
C
50µm
D
50µm
E
100µm
F
25µm
G
50µm
H
50µm
I
50µm
J
50µm
K
100µm
L
100µm

Figure 1

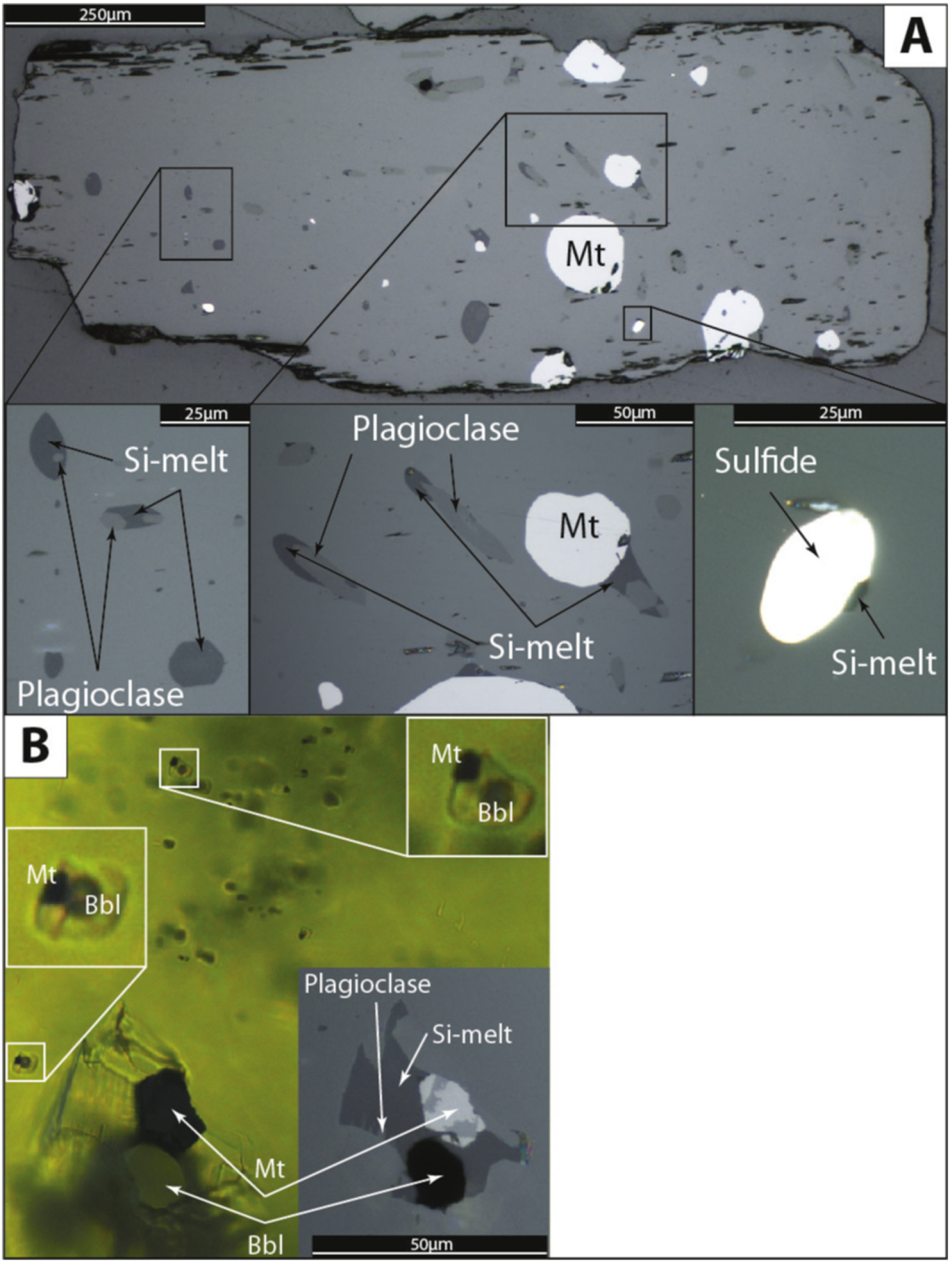
250µm
A
Mt
25µm
Si-melt
Plagioclase
50µm
Plagioclase
Mt
Si-melt
25µm
Sulfide
Si-melt
B
Mt
Bbl
Mt
Bbl
Plagioclase
Si-melt
Mt
Bbl
50µm

Figure 2

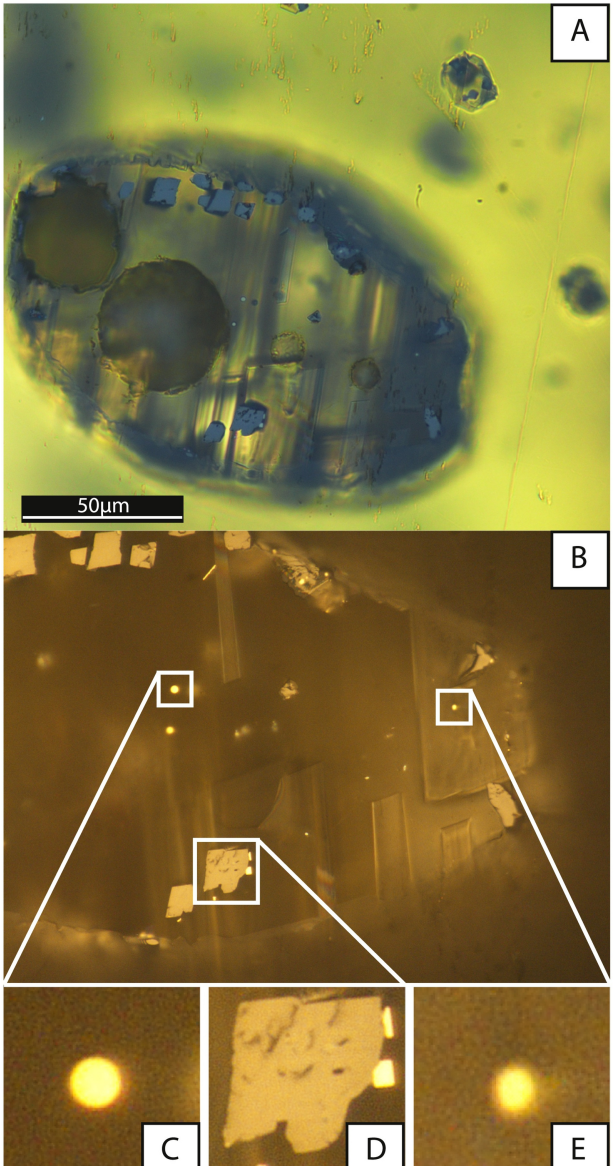

Figure 3

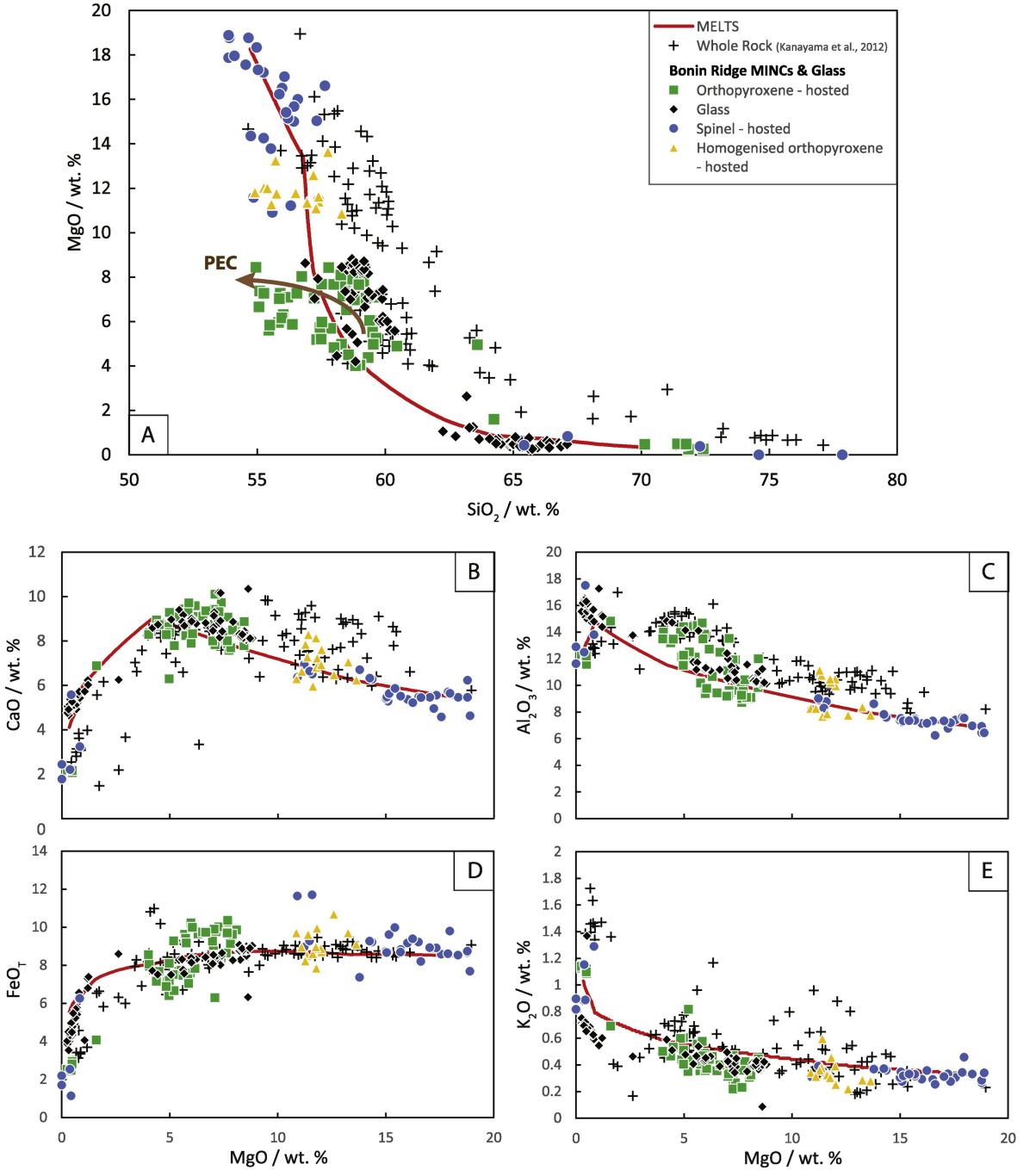
MELTS
Whole Rock (Kanayama et al., 2012)
Bonin Ridge MINCs & Glass
Orthopyroxene - hosted
Glass
Spinel - hosted
Homogenised orthopyroxene - hosted
PEC
A
MgO / wt. %
SiO2 / wt. %
B
CaO / wt. %
C
Al2O3 / wt. %
D
FeOT
E
K2O / wt. %
MgO / wt. %
MgO / wt. %

Figure 4

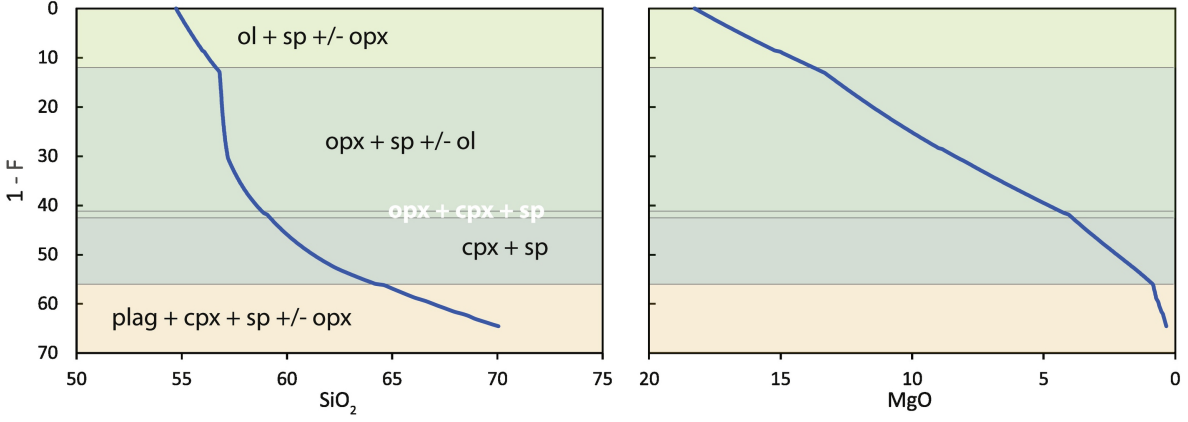
ol + sp +/- opx
opx + sp +/- ol
opx + cpx + sp
cpx + sp
plag + cpx + sp +/- opx
1 - F
0
10
20
30
40
50
60
70
50
55
60
65
70
75
SiO2
20
15
10
5
0
MgO

Figure 5

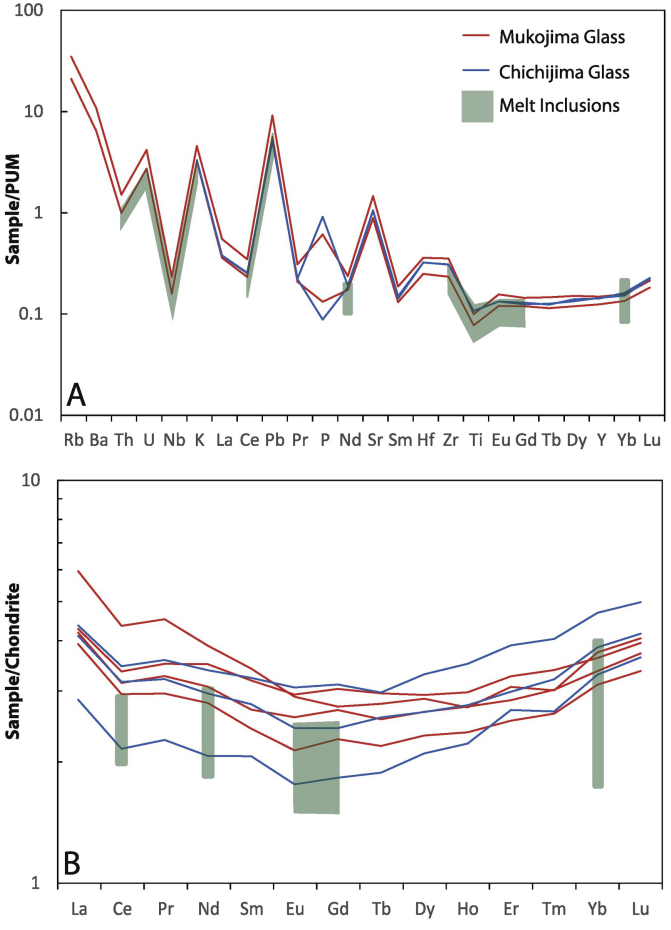
Mukojima Glass
Chichijima Glass
Melt Inclusions
Sample/PUM
100
10
1
0.1
0.01
A
Rb Ba Th U Nb K La Ce Pb Pr P Nd Sr Sm Hf Zr Ti Eu Gd Tb Dy Y Yb Lu
Sample/Chondrite
10
1
B
La Ce Pr Nd Sm Eu Gd Tb Dy Ho Er Tm Yb Lu

Figure 6

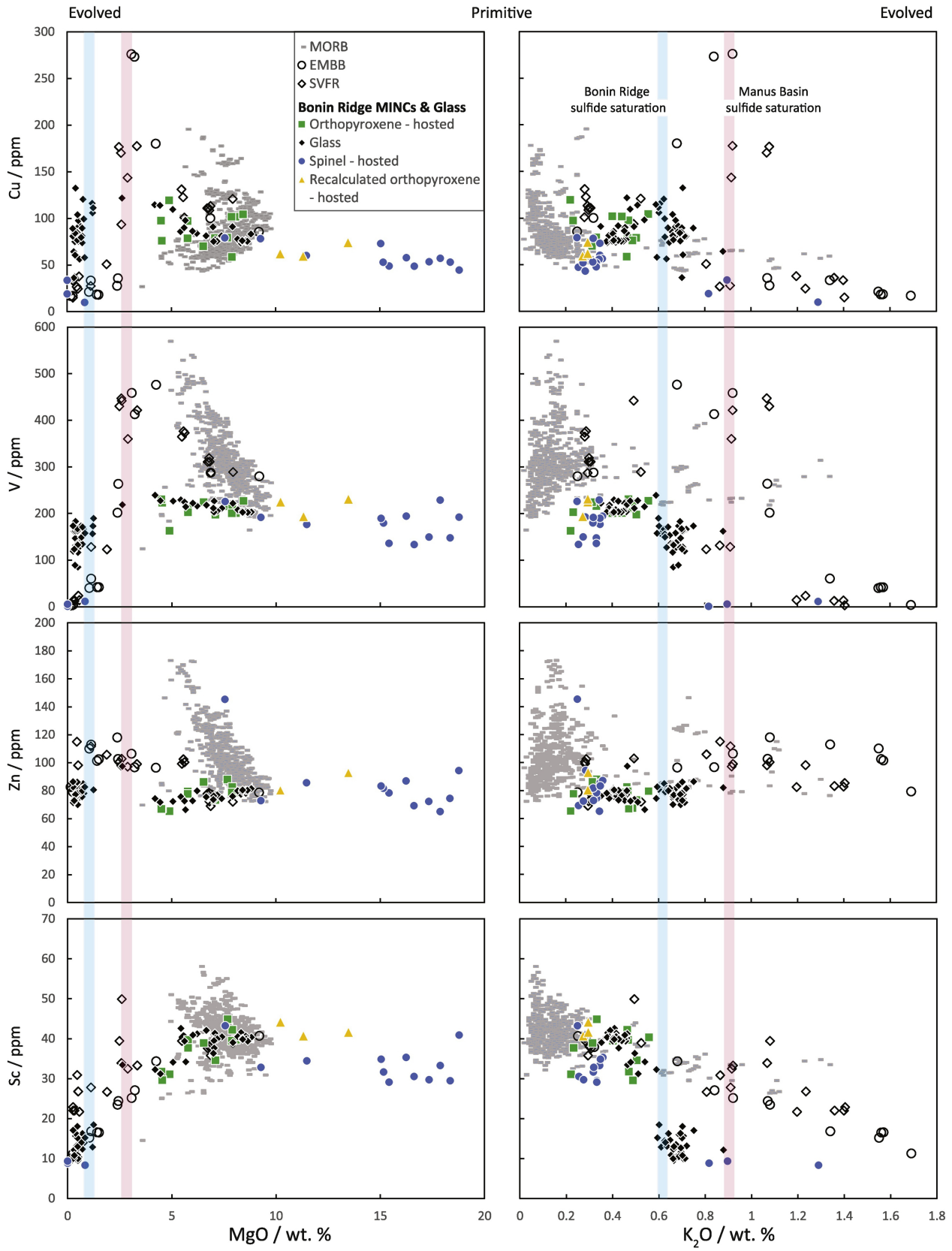
Evolved
Primitive
Evolved
MORB
EMBB
SVFR
Bonin Ridge MINCs & Glass
Orthopyroxene - hosted
Glass
Spinel - hosted
Recalculated orthopyroxene - hosted
Bonin Ridge sulfide saturation
Manus Basin sulfide saturation
Cu / ppm
V / ppm
Zn / ppm
Sc / ppm
MgO / wt. %
K2O / wt. %

Figure 7

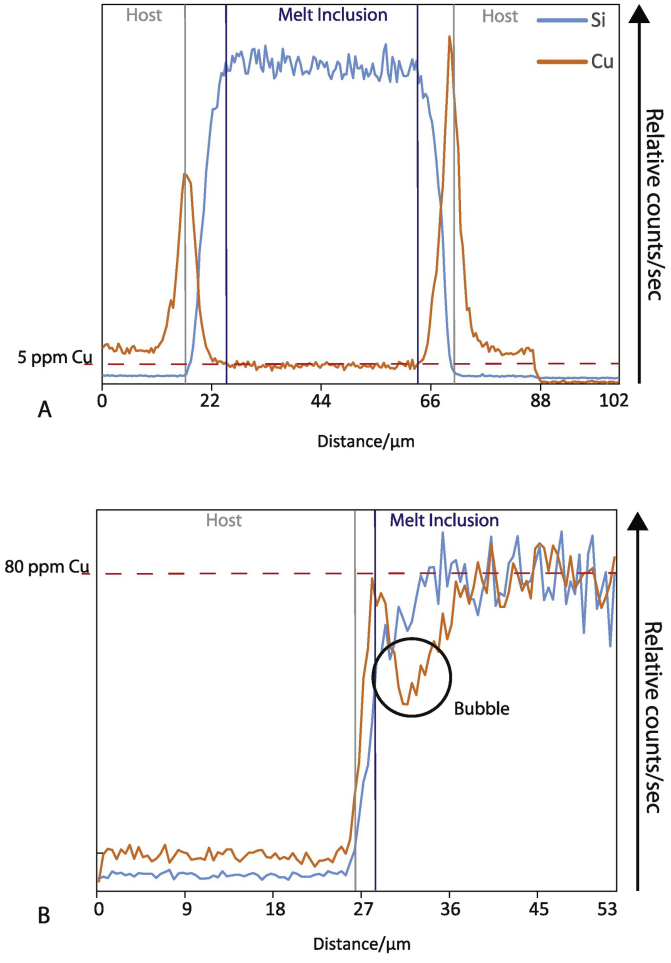
Host
Melt Inclusion
Host
Si
Cu
Relative counts/sec
5 ppm Cu
A
0
22
44
66
88
102
Distance/μm
Host
Melt Inclusion
80 ppm Cu
Bubble
Relative counts/sec
B
0
9
18
27
36
45
53
Distance/μm

Figure 8

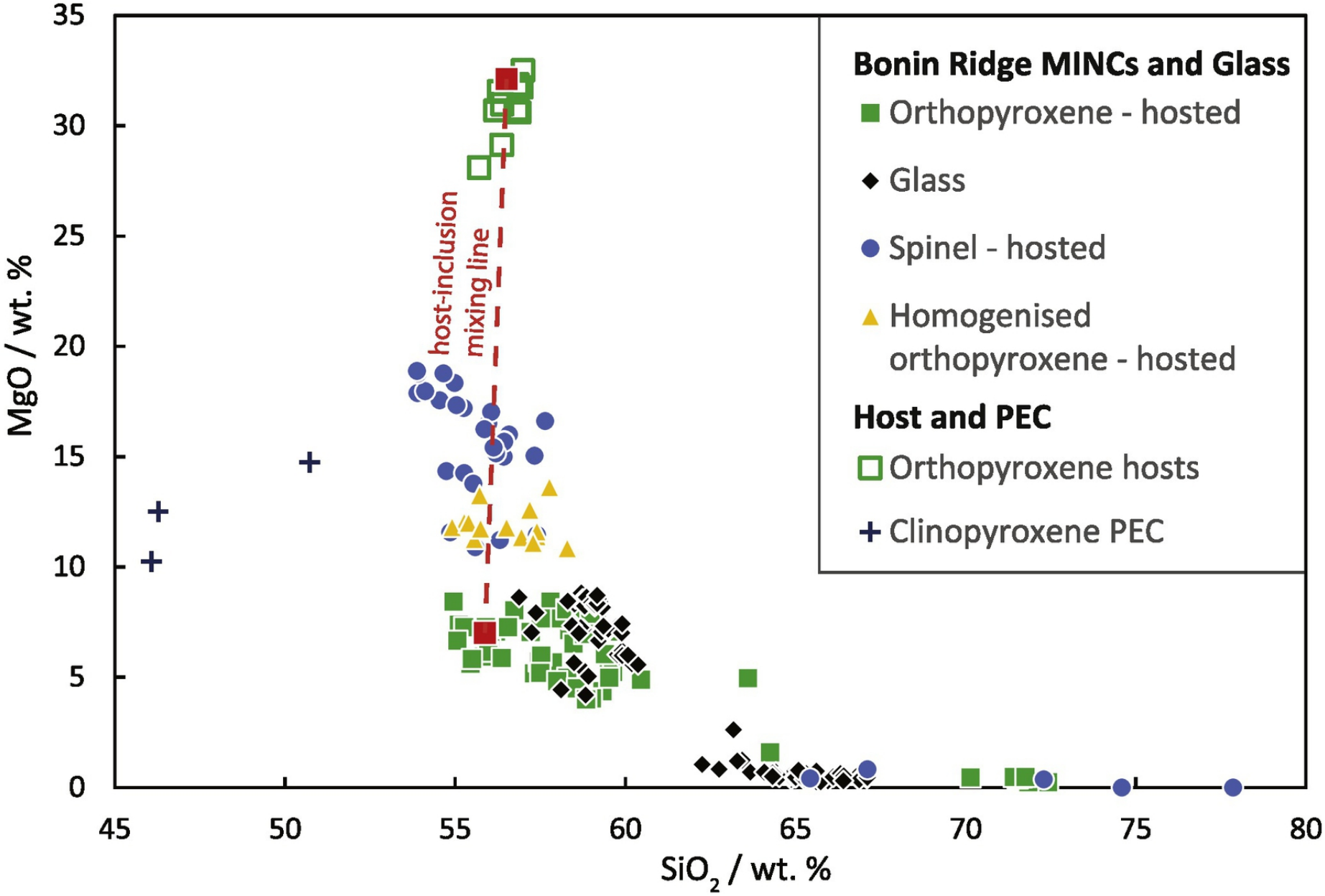
Bonin Ridge MINCs and Glass
Orthopyroxene - hosted
Glass
Spinel - hosted
Homogenised orthopyroxene - hosted
Host and PEC
Orthopyroxene hosts
Clinopyroxene PEC
host-inclusion mixing line
MgO / wt. %
SiO2 / wt. %
0
5
10
15
20
25
30
35
45
50
55
60
65
70
75
80

Figure 9

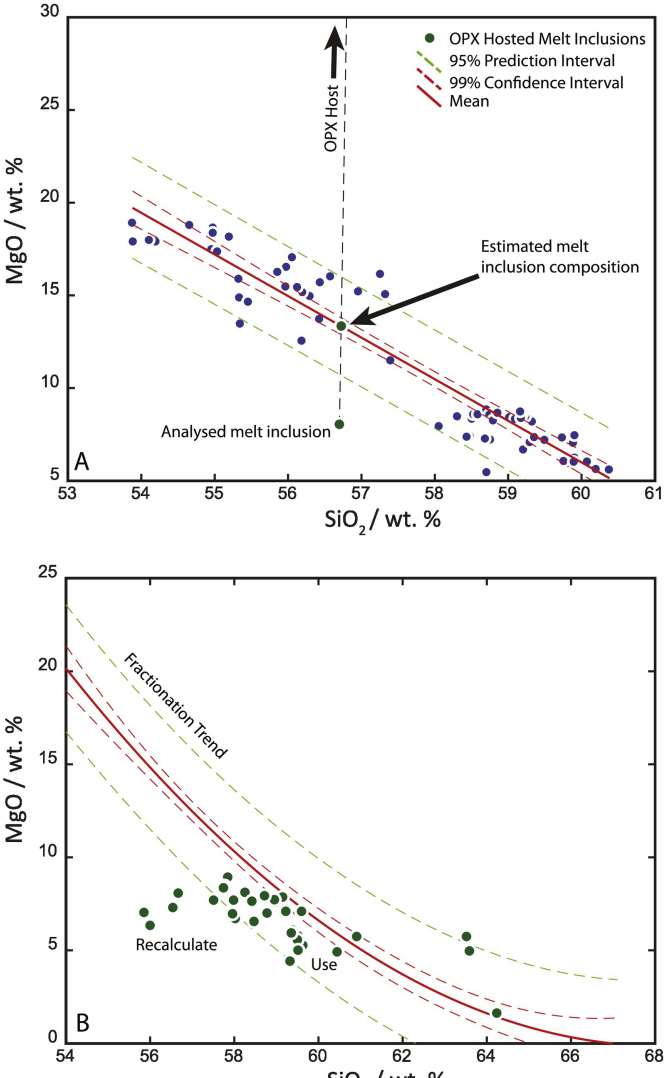
OPX Hosted Melt Inclusions
95% Prediction Interval
99% Confidence Interval
Mean
OPX Host
Estimated melt inclusion composition
Analysed melt inclusion
A
MgO / wt. %
SiO2 / wt. %
Fractionation Trend
Recalculate
Use
B
MgO / wt. %
SiO2 / wt. %

Figure 10

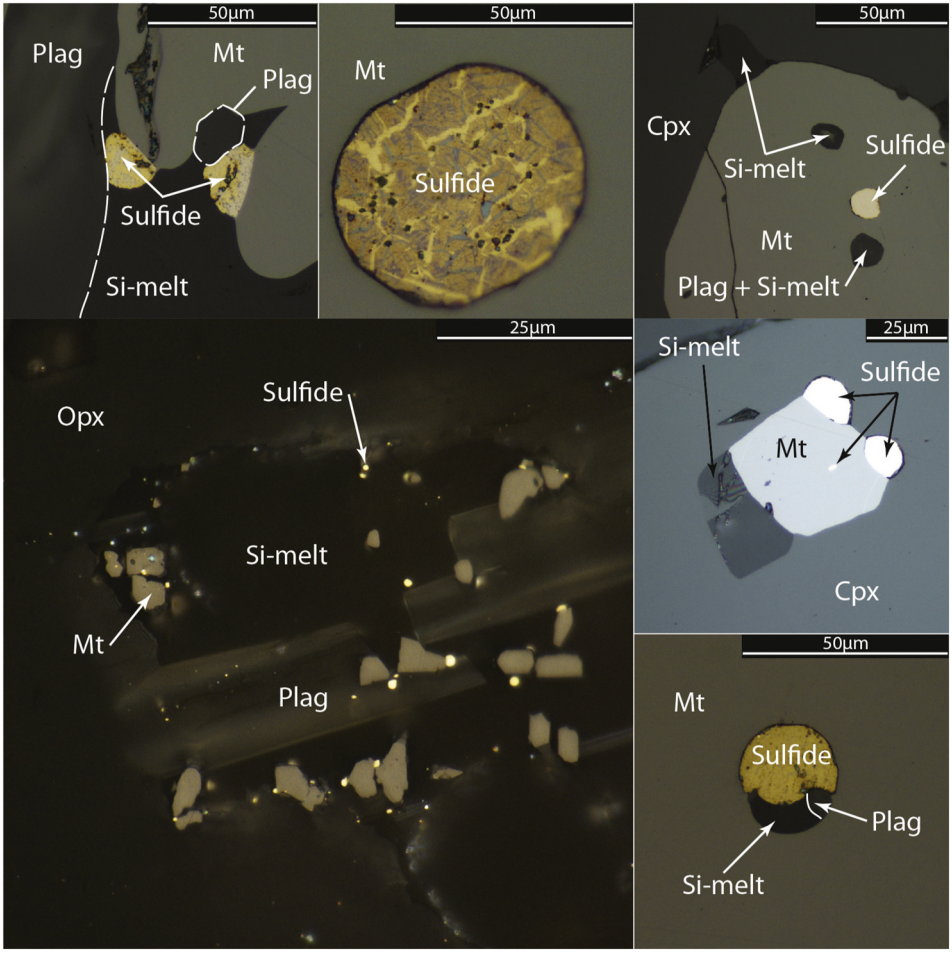
50µm
Plag
Mt
Plag
Sulfide
Si-melt
50µm
Mt
Sulfide
50µm
Cpx
Si-melt
Sulfide
Mt
Plag + Si-melt
25µm
Opx
Sulfide
Si-melt
Mt
Plag
25µm
Si-melt
Sulfide
Mt
Cpx
50µm
Mt
Sulfide
Plag
Si-melt

Figure 11

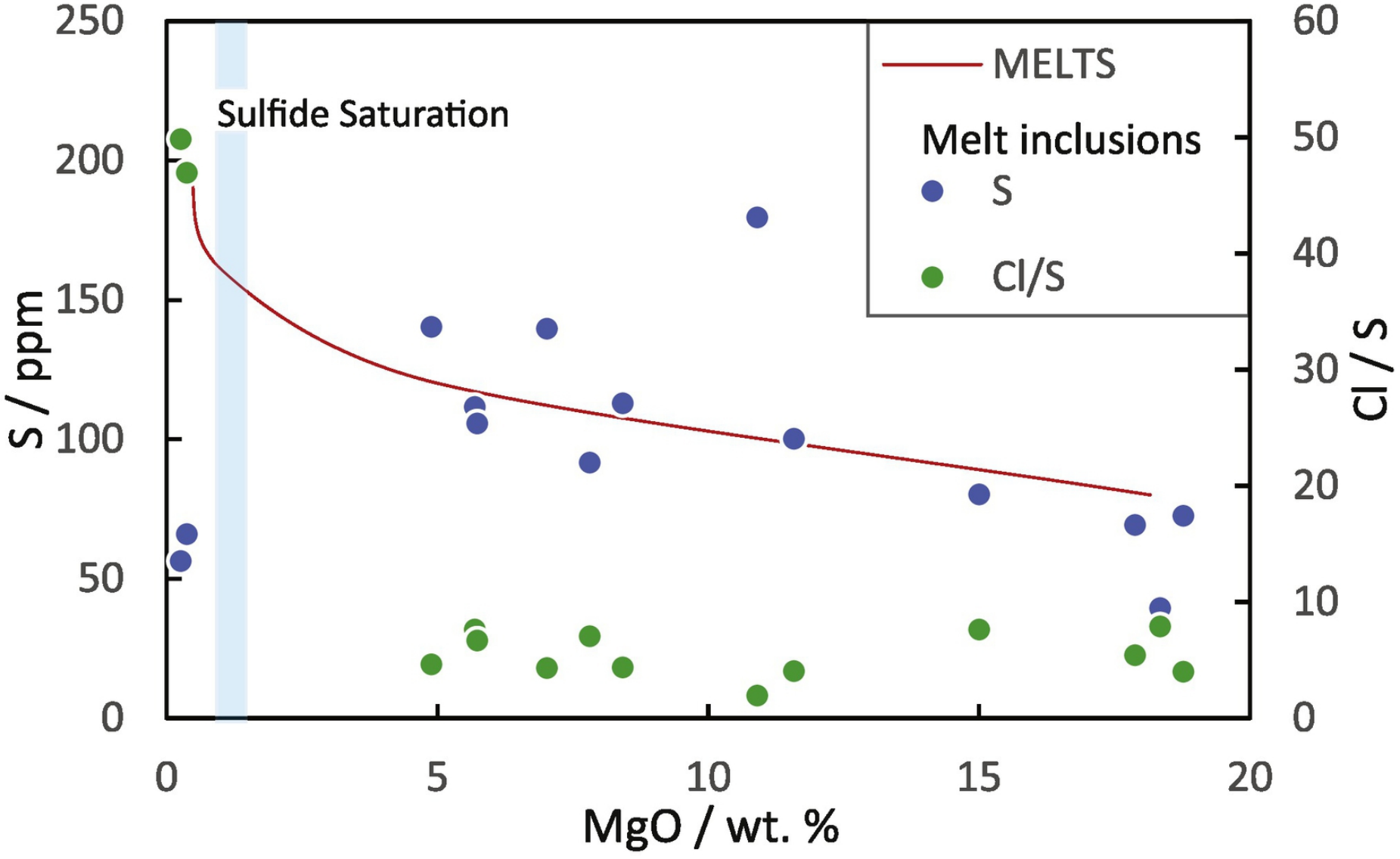
250
200
150
100
50
0
S / ppm
60
50
40
30
20
10
0
Cl / S
0
5
10
15
20
MgO / wt. %
Sulfide Saturation
MELTS
Melt inclusions
S
Cl/S

Figure 12